



HAL
open science

A new criterion to evaluate the machined surface quality of the Nomex® honeycomb materials

M. Jaafar, H. Makich, M. Nouari

► To cite this version:

M. Jaafar, H. Makich, M. Nouari. A new criterion to evaluate the machined surface quality of the Nomex® honeycomb materials. *Journal of Manufacturing Processes*, 2021, 69, pp.567-582. 10.1016/j.jmapro.2021.07.062 . hal-03325735

HAL Id: hal-03325735

<https://hal.univ-lorraine.fr/hal-03325735>

Submitted on 22 Aug 2023

HAL is a multi-disciplinary open access archive for the deposit and dissemination of scientific research documents, whether they are published or not. The documents may come from teaching and research institutions in France or abroad, or from public or private research centers.

L'archive ouverte pluridisciplinaire **HAL**, est destinée au dépôt et à la diffusion de documents scientifiques de niveau recherche, publiés ou non, émanant des établissements d'enseignement et de recherche français ou étrangers, des laboratoires publics ou privés.



Distributed under a Creative Commons Attribution - NonCommercial 4.0 International License

28 **Keywords:** Honeycomb; Nomex® material; Machining; New quality criterion; Surface quality

29 **1. Introduction**

30 Recent development projects for Airbus A350 or Boeing 787 Dreamliner confirm the increasing
31 use of the honeycomb materials for aeronautic fields, [1]. The research activities on honeycomb
32 core material are currently going through a new transition phase. Thus far, material properties
33 and mechanical and thermal behavior have been the dominant topics in this area of research.
34 With increasing applications, the production techniques of sandwich structures are subjected to
35 constraints and very high requirements from manufacturers. An important aspect of production
36 technology is honeycomb core machining. Honeycomb is the most popular core for sandwich
37 materials. It is chosen for its low density (about 5% compared to classical materials) and its good
38 mechanical performance. For these reasons, the core of rotor-blade for helicopters is
39 manufactured mainly by honeycomb materials, [2]. There are two wide variety of honeycombs,
40 metallic (aluminum or steel) and composite (Nomex® with glass fibers or carbon fibers). The
41 choice of honeycomb material depends on properties and the specific benefits of each material.

42 Nomex® honeycomb is the most non-metallic honeycomb core used in aerospace applications, it
43 is composed by phenolic resin impregnated aramid paper, [3]. Nomex® honeycomb, which
44 combines lightweight and a good mechanical behavior, is characterized by high out-of-plane
45 compression, shear properties and outstanding energy absorption characteristics. Also, various
46 studies have been conducted on mechanical properties of Nomex® honeycomb cores to
47 determine their behavior, [4–7]. These structures are characterized by their specific geometry.
48 The side length of honeycomb cell and its thickness are the most important geometric parameters

49 because they ~~decide~~ determine the mechanical behavior of the honeycomb material, [8–10].
50 Nevertheless, this material presents a forming challenge because of the geometric properties of
51 honeycomb structures. First of all, the uses of honeycomb material in sandwich composites is
52 limited by the difficulty of forming structures with complex geometries. Indeed, the two existing
53 methods for the manufacture of honeycomb allow to have only structures with parallelepiped
54 shape, [11,12]. Thus, a forming step by machining is necessary to obtain complex geometrical
55 shapes making the use of honeycomb materials possible in various fields. For example, the shape
56 of rotor blade of helicopter is so complex that the machining is the only way for obtaining
57 complex shapes on honeycomb material, [13]. However, there are some factors limiting
58 honeycomb machining, particularly the weakness of local bending stiffness of the cell walls and
59 the low density of honeycomb material itself. This shows the fragility of each cell-wall of the
60 honeycomb, which influences the quality of the obtained surfaces after the machining process,
61 [14]. To overcome this problem, Norvilie *et al.* [15] have used another material to filling cells of
62 honeycomb. They have used a frozen liquid to solidify the structure, [16]. Thus, for non-metallic
63 honeycomb, it is possible to use resin or expanses foam for the same goal. But, these method
64 require a long and intensive preparation, [15–20].

65 Several machining defects are observed when cutting Nomex®. Because of its composite nature,
66 uncut fibers is the most well-known machining defect [14,21]. Qin *et al.* [22] described this
67 defect by burr defect, they classified it in three categories according to their location and their
68 origin: (i)- Lumpy burr, (ii)- threadlike burr and (iii)- dotted burr. The same authors proposed
69 then an approach to remove burr data from scanning maps of each cell wall based on
70 dimensionality reduction and regression analysis. But these machining defects influence the
71 behavior of Nomex® in sandwich materials and their simple removal from the scanning maps

72 does not reflect the real existing machining defects. The poor quality of machined surface affects
73 the assembly of the sandwich materials, more precisely their presence generates a bad formation
74 of adhesive meniscus which has the role of the maintenance between the honeycomb and skins.
75 Indeed, a meniscus is created on both sides of the honeycomb, the latter ensures the proper
76 assembly of the sandwich material. A poor honeycomb surface quality causes dissymmetry of
77 this meniscus and the inclusion of air bubbles which cause peel failure of the whole sandwich
78 structure [23–25].

79 The malformation of meniscus causes adverse effects on the sandwich material, [26]. According
80 to Rion *et al.* [27], the optimum height of the adhesive meniscus is about 300 μm . This meniscus
81 height ensures a better maintenance of the assembly sandwich structure. Thus, the machining
82 defect must not exceed 300 μm to ensure that the cell-walls are completely between the meniscus
83 adhesive.

84 In this study, the treated issue concerns the machining operation by milling tool of a honeycomb
85 material. The use of ordinary cutting tools for machining honeycomb core usually generates a
86 poor surface quality or the impossibility of cutting walls of the honeycomb, [28]. These tools
87 produce generally tearing of fibers and delamination of cells. Subsequently, these cause a
88 reduction of bond strength between the skin and the honeycomb core, and thus a weaker joint for
89 composite sandwich structures. However, given the increasing use of this type of materials in the
90 industry, manufacturers have developed a specific tools for different machining operations of the
91 honeycomb core (grooving, surfacing, trimming, and drilling).

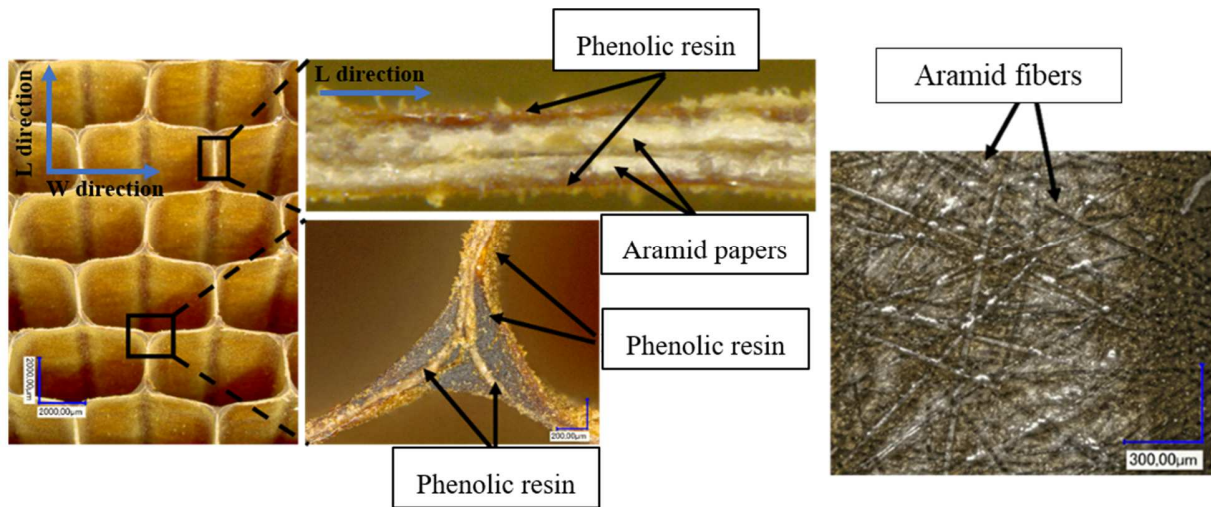
92 The literature review showed clearly that surface quality is one of the most important issue of
93 machining honeycombs. Due to the alveolar shape of honeycomb structures, the classical

94 measurement of the surface quality is not possible. The roughness for example cannot be
95 measured due to the lattice structure of honeycombs. In this paper, a new criterion was
96 developed to evaluate the surface quality for these kind of materials. A correlation between
97 surface quality and cutting conditions can then be made to optimize the cutting process of
98 honeycombs. Moreover, it is possible to carry out an in-depth analysis of the cutting conditions
99 influence as the feed rate and the spindle speed on the quality of obtained surfaces by machining
100 process. The final objective of this study is to understand the evolution of the honeycomb
101 materials machinability and the quantification of the induced cutting deflect.

102 **2. Experimental procedures**

103 *2.1. Description of the workpiece and cutting tool materials*

104 The workpiece material chosen for this study is Nomex® honeycomb with thin cell walls. The
105 Nomex ® honeycomb is made from aramid paper, it is produced from aramid fibers dipped in
106 phenolic resin (see Figure 1-a). The aramid fibers are distributed randomly in the Nomex® walls,
107 Figure 1-b. To form the honeycomb geometry of the honeycomb structure, the walls are
108 impregnated with phenolic resin. The honeycomb cores are made of continuous corrugated
109 ribbons of foil glued together in the direction L, Figure 1-a. The purpose of such a method is to
110 create a structure enabling to combine lightness and rigidity due to the hexagonal geometry of
111 the formed cells. Figure 2 summarizes the geometric characteristics of the honeycomb core.



112

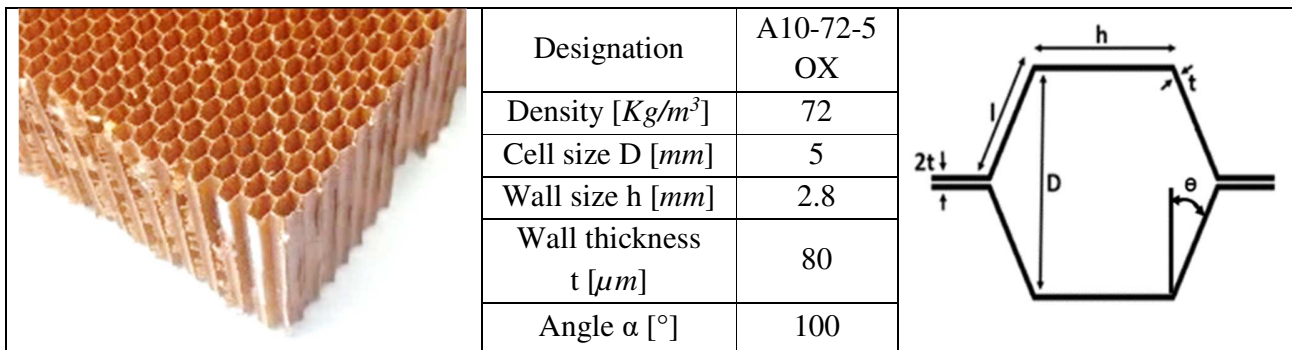
113

114 Figure 1. (a) Composition of the Nomex® honeycomb structure; (b) Quasi-random

115

116 distribution of aramid fibers.

117



118

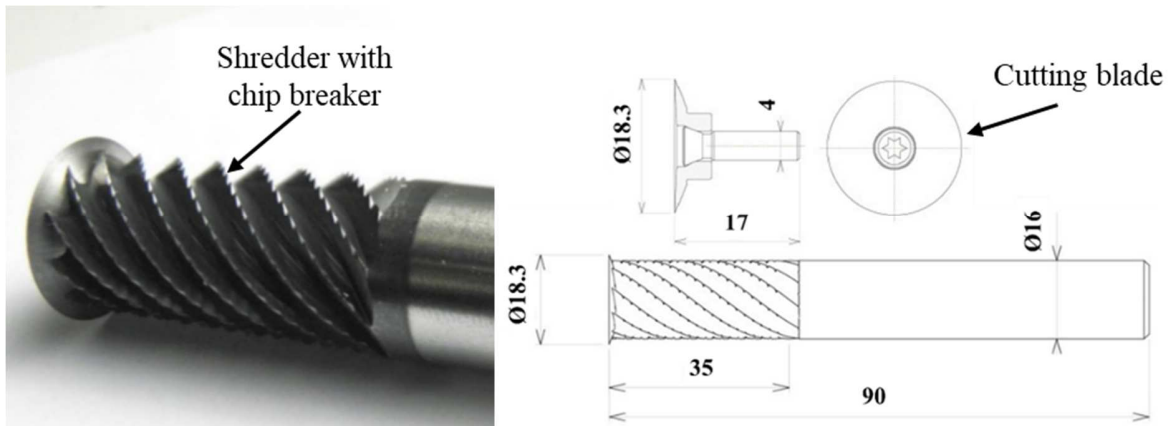
119 Figure 2. Geometric characteristics of the Nomex® honeycomb structure.

119

120 For our study, the milling cutters are provided by our partner 'EVATEC Tools' Company. The

120

main geometrical characteristics are described in Figure 3.



121

122 Figure 3. Milling cutter for Nomex® honeycomb. Evatec tools® reference: NACNA 011.

123 The selected milling cutter (Evatec tools® reference: NACNA 011) is a combined tool with two
 124 parts designed to surfacing and dressing machining operations. The first part is a cutter body
 125 made of high speed steel with 16 mm in diameter and having ten helix with chip breaker. This
 126 first tool part acts as a ‘shredder’ tool during the cutting of honeycombs. The second part is a
 127 circular cutting blade made of tungsten carbide with a diameter of 18.3 mm and having a rake
 128 angle of 22° and a flank angle of 2.5° (Evatec tools® reference: NAFNA 011). These two parts
 129 are mechanically linked to each other with a clamping screw.

130 *2.2. Experimental set up of milling tests*

131 All experimental milling tests showed in this paper were carried out on a three-axis vertical
 132 machining center Realmeca® RV-8. The main technical specifications of this machine are a
 133 maximum spindle speed of 24000 rpm, a power spindle motor of 30 KW, a maximum cutting
 134 feed of 20 m/min and a worktable area of 800 x 600 mm² (see Figure 4).

135 For assessing the performance of the machining process of Nomex® honeycomb, it is essential
136 to monitor and measure the cutting forces generated during cutting. Therefore, the cutting forces
137 were measured during the milling operation using Kistler dynamometer model 9129AA. The
138 Kistler table is mounted below the Nomex® honeycomb sample to measure the three
139 components of the machining force. Furthermore, during forces measurements, the x-axis of the
140 dynamometer is aligned with the feed direction of the milling machine and the longitudinal
141 direction of the workpiece (parallel to core ribbons and the direction of honeycomb double wall).



142

143

Figure 4. Experimental test setup.

144

145 To identify the influence of cutting conditions on the milling operation, several parameters were
146 chosen. Milling conditions are summarized in Table 1. To study the quality of the machined
147 surface and its relationship with the machining conditions, four spindle speeds combined with
148 four feed rates were chosen. As mentioned above, only few studies of honeycomb core
149 machinability have been found in the literature. So, there is no indication for the selection of

150 optimal cutting conditions. This study was then firstly focused on the identification the most
151 influencing cutting conditions which allow to obtain the better machined surface quality.

152 Table 1. Cutting conditions for milling tests.

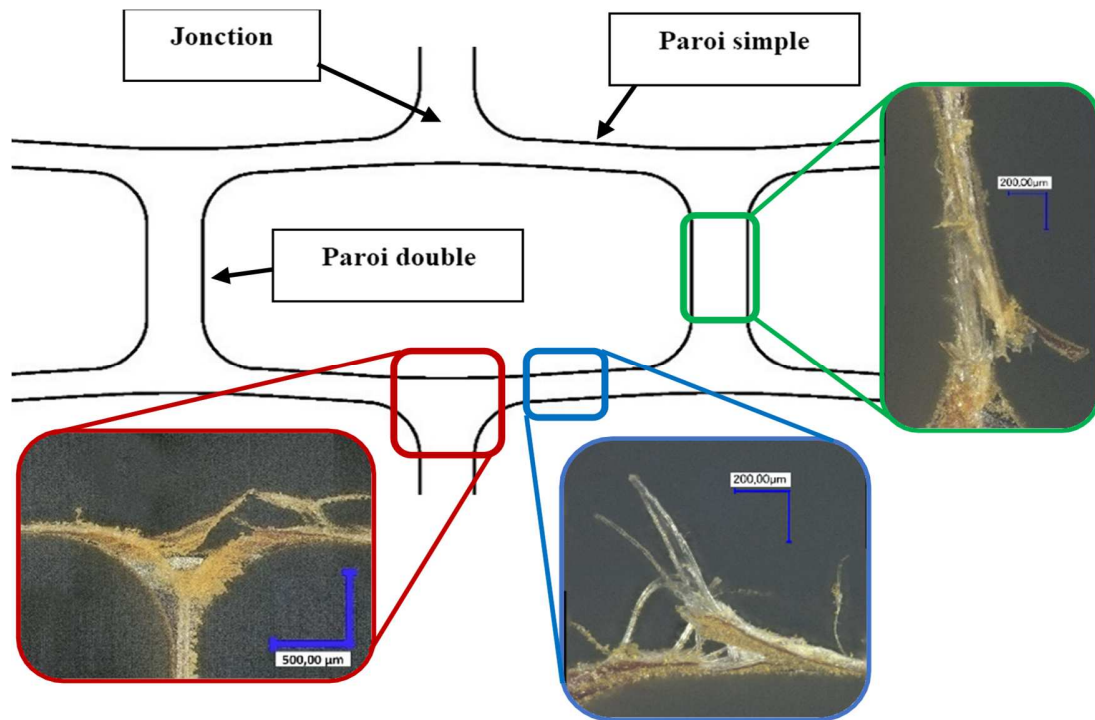
Spindle speed N (rpm)	2000	10000	15000	23000
Feed rate f (mm/min)	150	1000	1500	3000

153

154 3. Results and discussion

155 3.1 Analysis of induced cutting defects

156 The milling operation may involve damage around and in depth of the machined area such as
157 tearing of fibers, delamination of the walls, thermal degradation (overheating), torn wall and
158 uncut fibers, etc. As mentioned above, the quality of the surfaces is of crucial importance. Figure
159 5 shows the main areas of machining defects occurrence. These defects are observed for simple
160 walls and characterized by a very thin thickness. They include tearing of simple walls and uncut
161 fibers. The double walls are more resistant to tearing because they are thicker and contain an
162 extra layer of resin that bonds the two walls. The most pronounced defect in the double wall
163 zone is the presence of uncut fibers. The junction zones, which represent the meeting point of
164 several walls, are characterized by the existence of a larger quantity of resin. They undergo
165 delamination which results in the separation of the walls and the deterioration of the resin.



166

167

Figure 5. Different cutting defects observed on the Nomex® honeycomb samples.

168

169

170

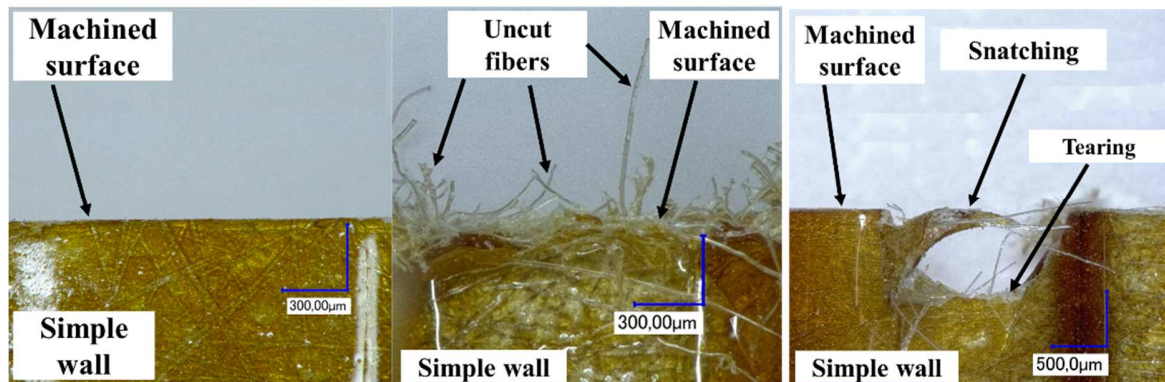
171

172

173

Figure 6 shows examples of simple surface walls generated during milling with different conditions. Optical images compare good machining (Figure 6.a) with two other extreme situations with bad machining (Figures 6.b and 6.c). The uncut fibers exceed the machined surface with different lengths and orientations (the fibers constituting the Nomex® paper are short and randomly mixed), Figure 6.b. In the latter case, snatching and tearing of the wall are observed, see Figure 6.c.

174



175

176

177

(a) (b) (c)
Figure 6. Different cutting defects observed on the Nomex® honeycomb.

178 The bad machining of Nomex® honeycomb materials is characterized by the appearance of
179 tearing in the cell walls and uncut aramid fibers. These defects constitute all the shape defects.

180 The shape defect is a first-order defect of a size ranging from a few tens micrometers to few
181 millimeters. The determination of this defect is of paramount importance to validate the use of
182 this type of material as being the core material of sandwich materials. This defect has a direct
183 effect on maintaining the assembly of the sandwich structure and its appearance often causes
184 anomalies during the formation of adhesive menisci on both sides of the honeycomb walls, [27].

185 These menisci maintain the assembly of the sandwich material. Thus, the defects observed
186 during the machining of Nomex® are qualified as flatness defects.

187 3.2. Description of the surface quality quantification

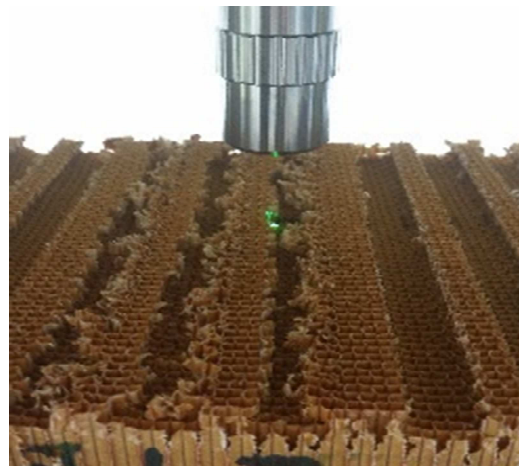
188 The quality of the machined surface depends on several parameters (cutting conditions, tool
189 geometry, vibration of the machine-tool, etc.). Composite materials are characterized by the

190 appearance of uncut fibers, tearing of the material particles or debris and the resin thermal
191 degradation, [29–34]. Generally, the machining defect is quantified by measuring the roughness.
192 In our case study, the measurement of the roughness gives erroneous results of the surface
193 quality for two reasons, the first reason is due to the thin walls of the honeycombs and the second
194 is caused by the important number of uncut fibers on the machined surface. The calculated
195 roughness then represents the roughness of the surface of uncut fibers. If the quality is poor
196 (uncut fibers and tearing) but the surface of fibers is smooth, we will obtain low roughness which
197 does not represent the real quality of the machined surface. Hence the implementation of a more
198 reliable method is strongly needed to characterize and quantify these defects.

199 The qualification and quantification of the machined surface quality was realized through
200 programming on Matlab software. During the implementation, the key technical steps are the (i)-
201 3D scanning of the machined surface, (ii)- the implementation of a least squares plane and (iii)-
202 the determination of planarity defects. All these steps will be specified in the following
203 paragraph.

204 The first step is to digitize the machined surface and extract the cartesian coordinates of each
205 point (x_i, y_i, z_i) with $i = 1$ to n (n is the number of measured points). The digitization of the
206 machined surface is performed with the 3D interferometer equipment, see Figure 7.a. The
207 measurement technique of the 3D optical microscope profilometer is based on the principle of
208 white light interferometry. This is a non-contact measuring system that offers many advantages
209 for morphological characterization via three-dimensional (3D) images, with rapid acquisition,
210 and unequaled data richness (profiles, surface conditions, ...). This equipment makes it possible,
211 in the case of our work, to produce topographies of 3D surfaces with high resolution. The 3D

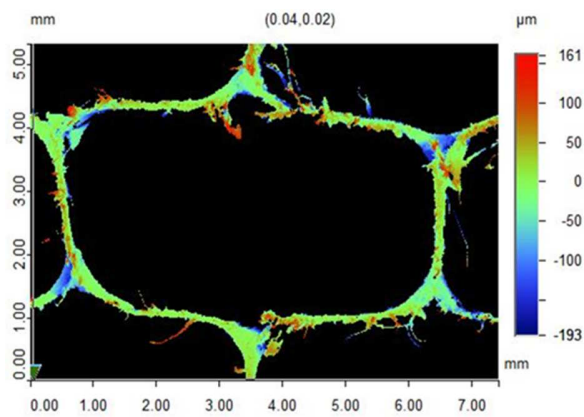
212 interferometer was used in this study to perform three-dimensional measurements quickly and
213 easily on machined surfaces with extreme vertical resolution (<0.1 nm), depending on the
214 objective and a good lateral resolution. This measurement makes it possible to obtain the 3D
215 distribution of the various surface defects in the space and locate them well through clouds of
216 points in the cartesian coordinate system (x, y, z) , Figure 7.b.



217

218

(a)



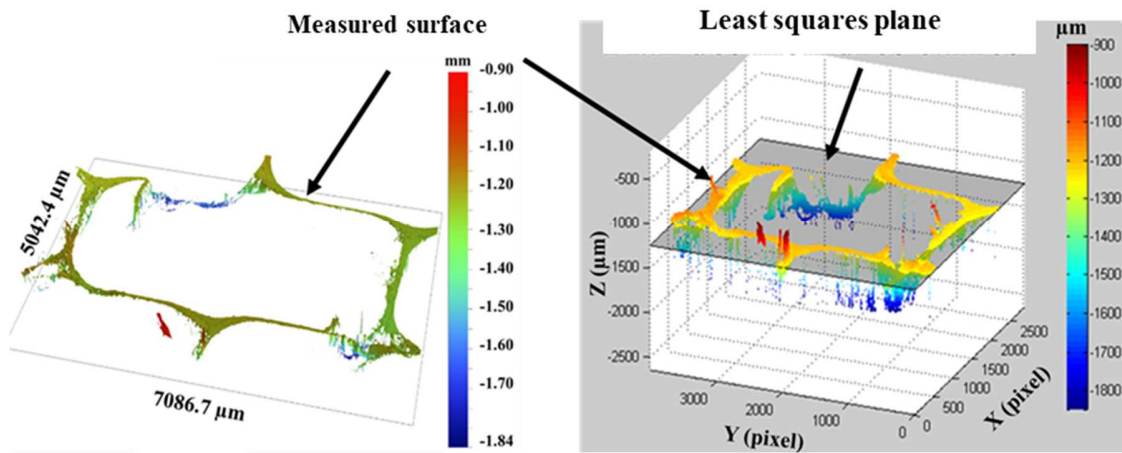
219

220

(b)

221 Figure 7. (a) Measuring of the machined surface quality of Nomex® samples. (b) Scanned
222 surface using the 3D interferometer technique.

223 Several methods are standardized to quantify unevenness. Among these methods we can find: (i)
 224 the association by a plane passing by three points, and (ii) the association by a least squares
 225 plane. the second method was used in this study which consists in determining the plane of the
 226 least squares of the surface points to be measured, it is the plane closest to all the points of the
 227 surface. After having determined this plane, it possible to identify the distance separating this
 228 plane at the two distant points on either side of this same plane, Figure 8. This method is
 229 considered as the most accurate method.



230

231

(a)

(b)

232 Figure 8. (a) Digitized surface using the 3D interferometer. (b) Processing the flatness error
 233 measured by inserting the least squares plane.

234 The least squares plane is defined by an equation (Eq. (1)) of a plane in the same cartesian
 235 reference frame :

$$236 \quad z = f(x, y) = ax + by + c \quad (1)$$

237 The error or the deviation calculated between the desired plane $f(x_i, y_i)$ and a point on the
 238 scanned surface z_i is defined by Eq. (2) :

239 $e_i = |f(x_i, y_i) - z_i|$ (2)

240 with $i=1$ to n (n is the number of measured points). Thus, the goal is to minimize the function S .

241 S is the sum of the squares of the deviations calculated for each set of points (x_i, y_i) , S is a

242 polynomial of degree 2 :

243
$$S(a, b, c) = \sum_{i=0}^n e_i^2 = \sum_{i=1}^n (ax_i + by_i + c - z_i)^2$$
 (3)

244 By minimizing the function S , we minimize the distance between the different points of the

246 scanned surface and the plane to be constructed. It is necessary to remember the definition of the

247 least squares plane which is the closest plane to all measured points, from where it is necessary

248 to identify the different parameters of this plane (a, b, c) by solving these three equations:

249
$$\frac{\partial S(a, b, c)}{\partial a} = 0$$

250
$$\frac{\partial S(a, b, c)}{\partial b} = 0$$
 (4)

251
$$\frac{\partial S(a, b, c)}{\partial c} = 0$$

252 The system of equations below (Eq. (4)) can then be solved to determine the parameters (a, b, c)

253 :

254
$$\begin{pmatrix} \sum_i x_i^2 & \sum_i x_i y_i & \sum_i x_i \\ \sum_i x_i y_i & \sum_i y_i^2 & \sum_i y_i \\ \sum_i x_i & \sum_i y_i & n \end{pmatrix} \begin{pmatrix} a \\ b \\ c \end{pmatrix} = \begin{pmatrix} \sum_i x_i z_i \\ \sum_i y_i z_i \\ \sum_i z_i \end{pmatrix}$$
 (5)

255 A least squares plane is determined for each machined surface. Thus, the distance between the

256 least squares plane and each point of the measured surface is calculated (d_i^{sup} : distance between

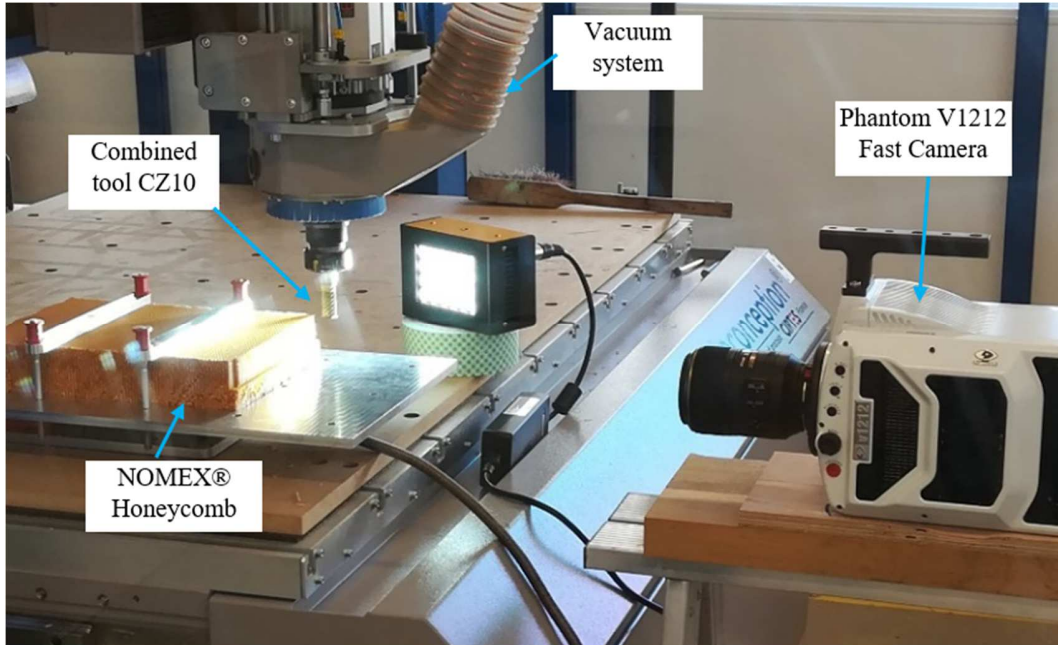
257 the least squares plane and a point located above; d_i^{inf} : distance between the least squares plane
258 and a point located below). The defect of flatness P is then determined through the following
259 equation:

$$260 \quad P = \max(d_i^{sup}) + \max(d_j^{inf}) \quad (6)$$

261 The method presented above was carried out on Matlab® software. It allowed to determine the
262 flatness defect for each machined surface with high precision.

263 *3.3. Analysis of the chip formation process when milling honeycomb structures*

264 During the material removal in machining operations, the chip formation process involves strong
265 interactions between the cutting tool and the material being machined. Chip formation is directly
266 conditioned by the behavior of the material and the geometry of the cutting tool, and by the
267 selected cutting conditions (rotational speed, cutting speed, feed rate, ...). To study the
268 interactions between the tool and the structure during machining, fast video camera (Phantom
269 V1212) was used to follow the chip formation process at different stages, Figure 9.



270

271

Figure 9. Chip formation monitoring device with fast video camera.

272

The machining tool is characterized by a difference in diameter between the circular cutting

273

blade and the shredder. This causes chip formation in several stages. The cutting blade is the first

274

component of the tool that encounters the honeycomb walls, Figure 10.a. Chip formation is

275

initiated by cutting the walls with the cutting blade. The rotation and the advance of the blade

276

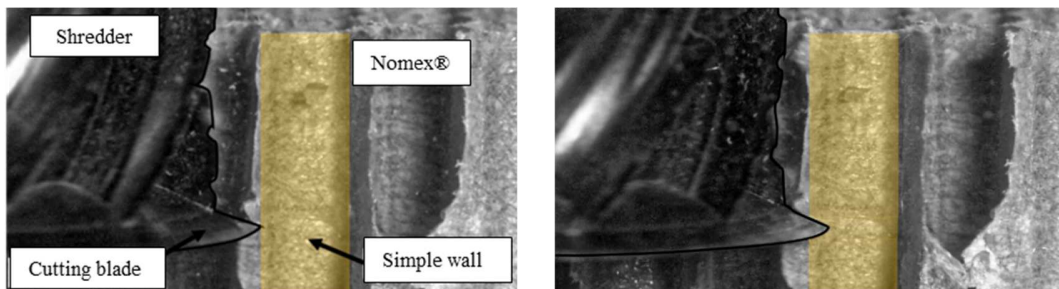
cause friction between the cutting blade and the walls, and then leads to a separation process of

277

the wall into two parts. The cut part of the wall continues to rub on the upper surface of the

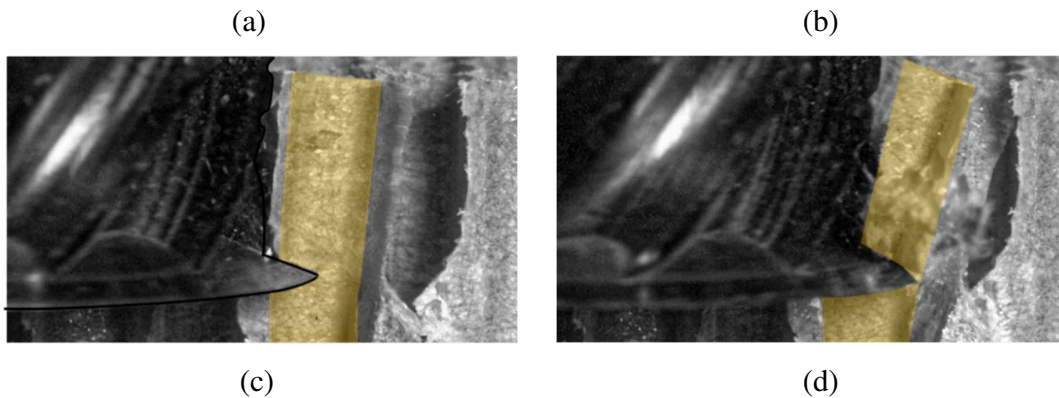
278

cutting blade until it reaches the cutter body (the shredder), Figure 10.b and 10.c.



279

280



281

282

283

284

285

Figure 10. Chip formation mechanisms during the machining of Nomex® material. The selected cutting conditions are the feed $f = 1000$ mm / min and spindle speed $N = 15000$ rpm.

286

287

288

289

290

291

292

293

294

295

296

297

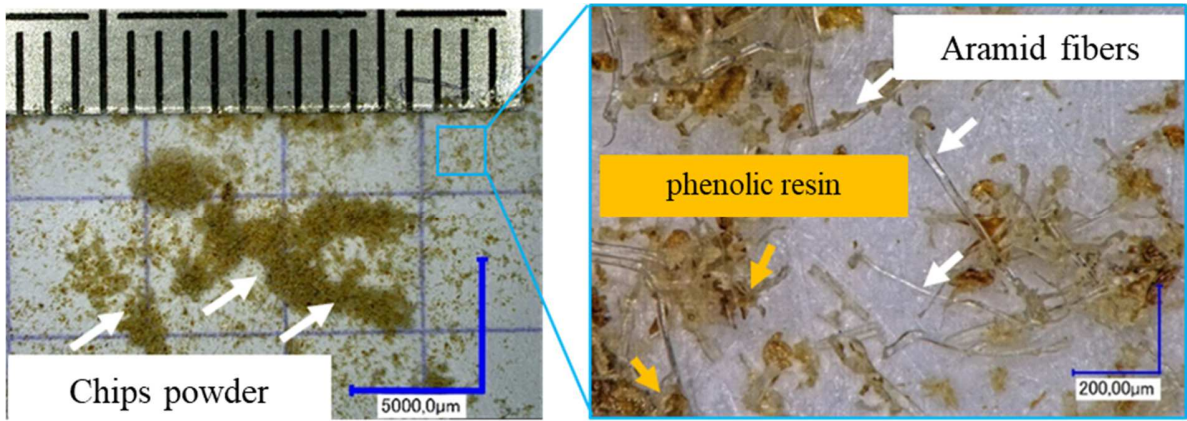
298

299

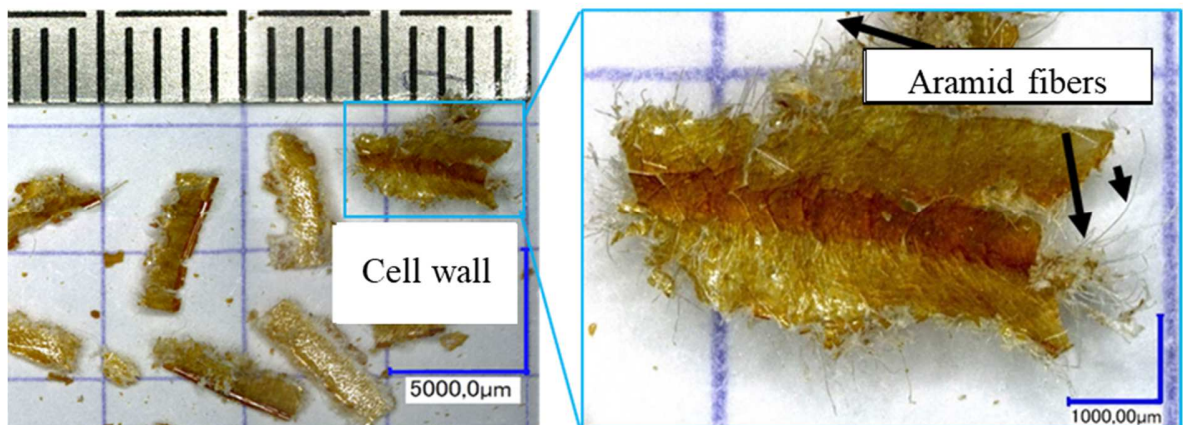
300

The total chip formation is done once the previously cut walls are shredded and pushed back by the upper part of the tool, Figure 10.d. The upper surface of the cutting blade represents the cutting face. The chip separated from the walls slides on the cutting blade before reaching the shredder. The lower surface of the cutting blade represents the flank face since it is in contact with the freshly machined surface. After the Nomex® honeycomb has been machined, there are different forms of chips. The combined action of the cutting blade and the shredder causes, depending on the machining conditions, dust chips or chunks of the cell walls of the structure. Figures 11-14 show some examples of the Nomex® honeycomb chips obtained after machining. The resulting milling chips with high spindle speeds ($N = 23000$ rpm) and low feed rate ($f = 200$ mm/min) are in the form of powder consisting of aramid fibers and phenolic resin cut into fine particles less than $100 \mu\text{m}$ in size, Figure 11. By increasing the feed rate (3000 mm/min), the morphology of the chip completely changes. The chip is observed in the form of walls with a width of 1 mm and a length going from 4 to 6 mm, Figures 12. Larger size chips are generated at low spindle speeds (2000 rpm), these walls are indeed torn cells and traces of tearing are observed, Figures 13. The fourth category of chips is observed with low spindle speeds and high

301 feed rates ($N = 2000$ rpm and $f = 3000$ mm / min), these are whole cells generated as a chip
 302 during the machining, sets of 2 to 3 cells are observed, Figure 14.



303 (a) (b)
 304 Figure 11. Nomex® chip morphology for $N = 23\ 000$ rpm and $f = 200$ mm / min: (a) chips in
 305 the form of yellow dust, (b) composition of the chip (aramid fibers and phenolic resin).
 306
 307



308 (a) (b)
 309 Figure 12. Nomex® chip morphology for $N = 23\ 000$ rpm and $f = 3000$ mm / min: (a) chips in
 310 the form of Nomex® walls, zoom on a cut wall.
 311
 312

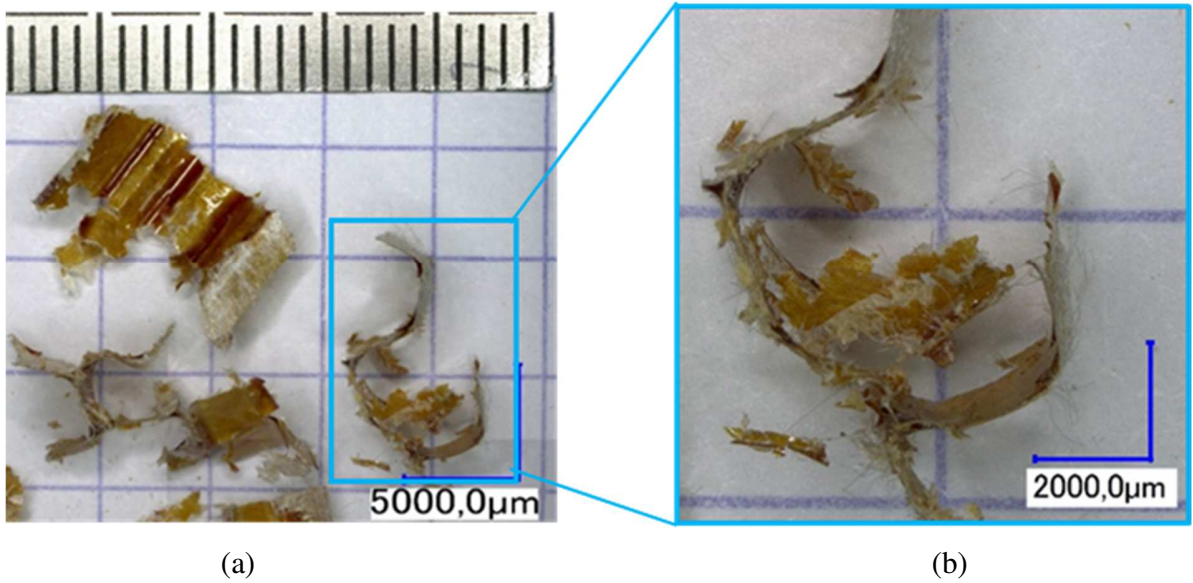


Figure 13. Nomex® chip morphology for $N = 2000$ rpm and $f = 200$ mm / min: (a) chips in the form of several Nomex® walls, (b) Zoom on the cut walls

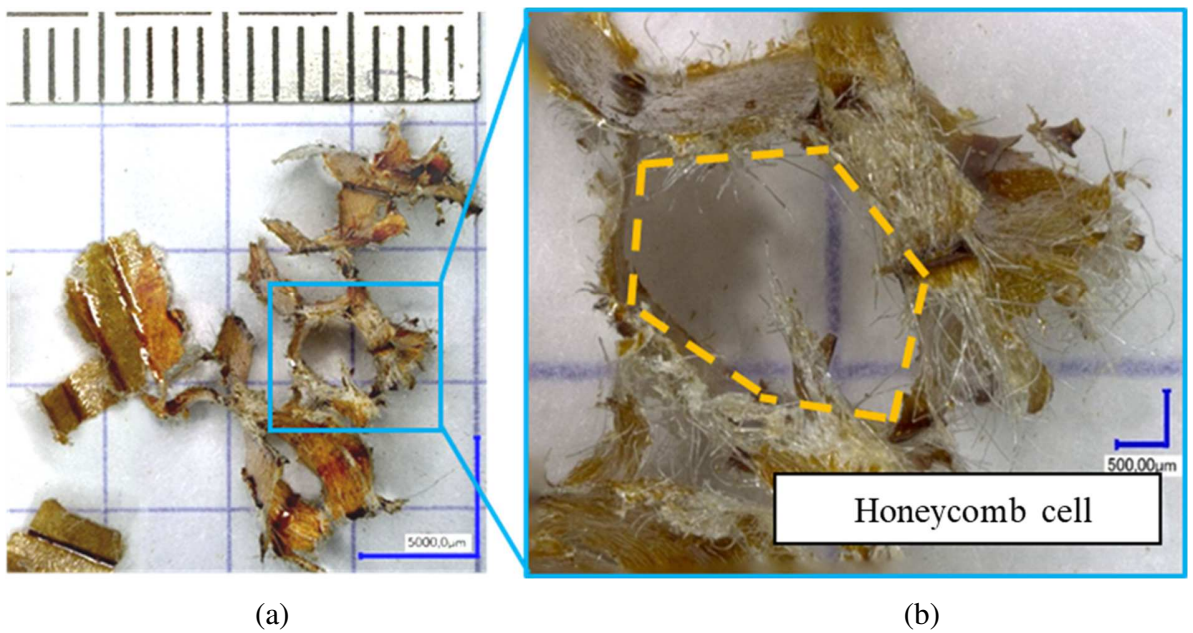
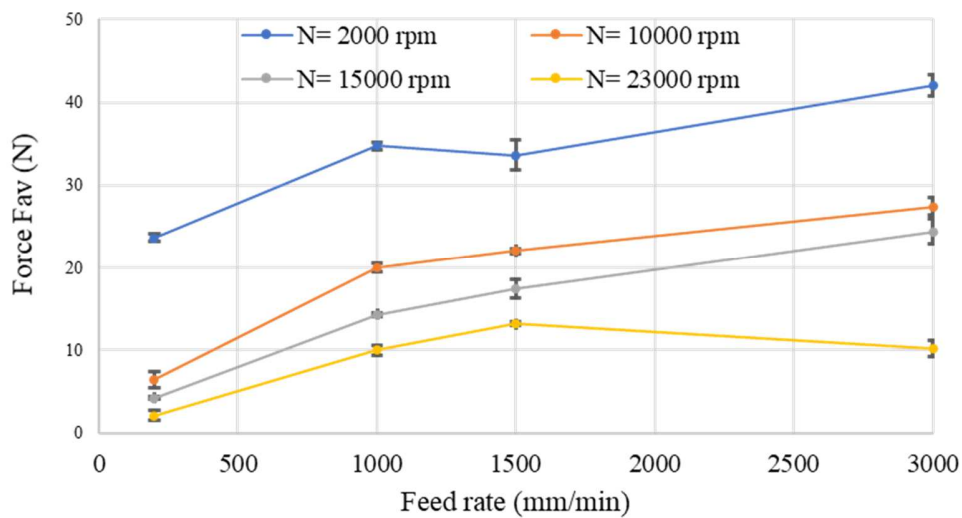


Figure 14. Morphology of Nomex® chips for $N = 2000$ rpm and $f = 3000$ mm / min: (a) chips in the form of Nomex® cells, (b) zoom on the cut cell.

322 3.4. Analysis of the milling cutting forces

323 Figures 15 and 16 show the evolution of the average cutting force F_{av} and the different
324 components of the cutting force (F_x , F_y and F_z) depending on the selected machining condition.
325 In general, there is a low level of effort generated during milling of the Nomex® honeycomb.
326 The average cutting force does not exceed 50 N, it is much lower than usual values observed for
327 classical composite materials where the forces are of the order of 150-300 N, [35]. This low
328 effort can be explained by the low density of the material (about 5%) and the alveolar structure
329 of honeycomb. This is also observed for the cutting force components F_x which is not the
330 dominant force as for the machining of standard composite materials. The tool, during its
331 trajectory, meets only thin walls forming the alveolar structure of the honeycomb.



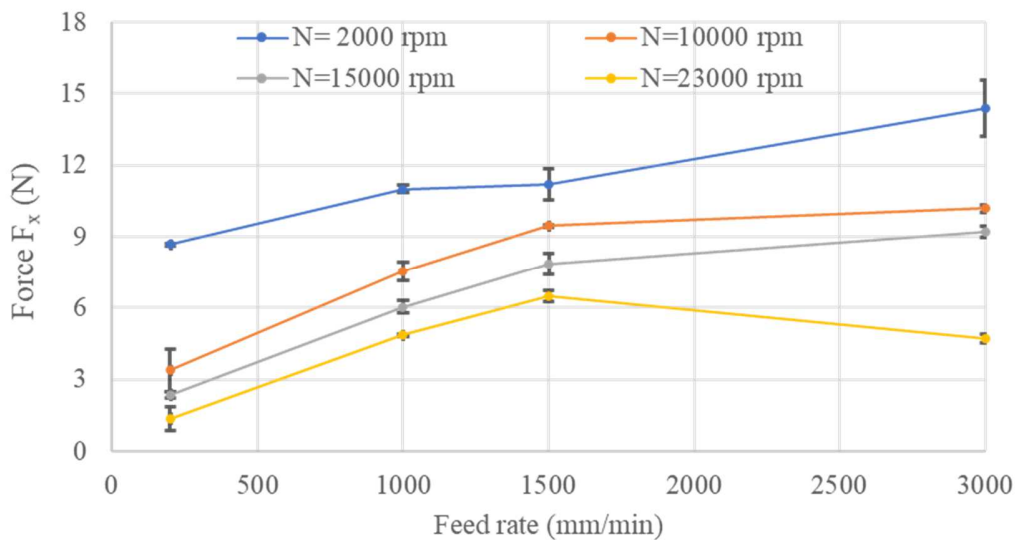
332

333 Figure 15. Evolution of the average cutting force F_{av} for different cutting conditions.

334 Comparing the three components of the cutting force in Figure 16, the F_z force is the highest
335 force. It is twice as high as F_x and F_y . This difference is linked to the mechanical behavior of the

336 honeycomb which is considered to be an orthotropic behavior, and which therefore depends on
337 the loading direction.

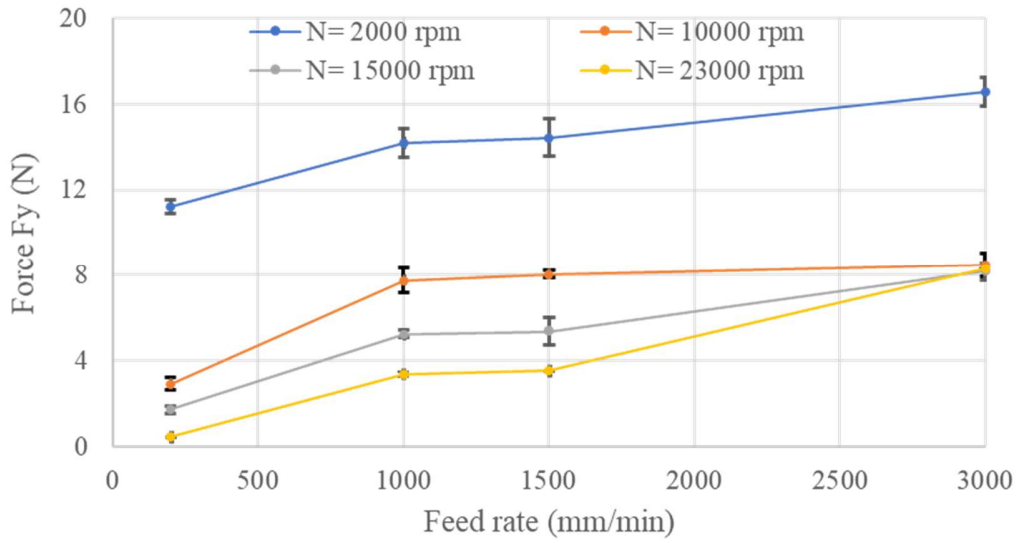
338 The maximum forces are observed for low spindle speeds and high feed rates. The cutting force
339 decreases with increasing the spindle speed. For a feed rate of 3000 mm/min, the cutting force
340 reaches the value of 10 N at a spindle speed of 23000 rpm. Reducing the feed rate also lowers
341 the cutting force. A decrease of 20 N is observed between the feed rate 3000 mm/min and 200
342 mm/min at a spindle of 2000 rpm. The minimum force is observed for a high rotation speed
343 (23000 rpm) and a low feed rate (200 mm/min). The same trend is observed for all components
344 of the forces which increase with the feed rate and decrease with the spindle speed. The response
345 of honeycomb structures to the stresses of machining is influenced by their viscoelastic behavior
346 sensitive to the effect of loading speed, [37,49].



347

348

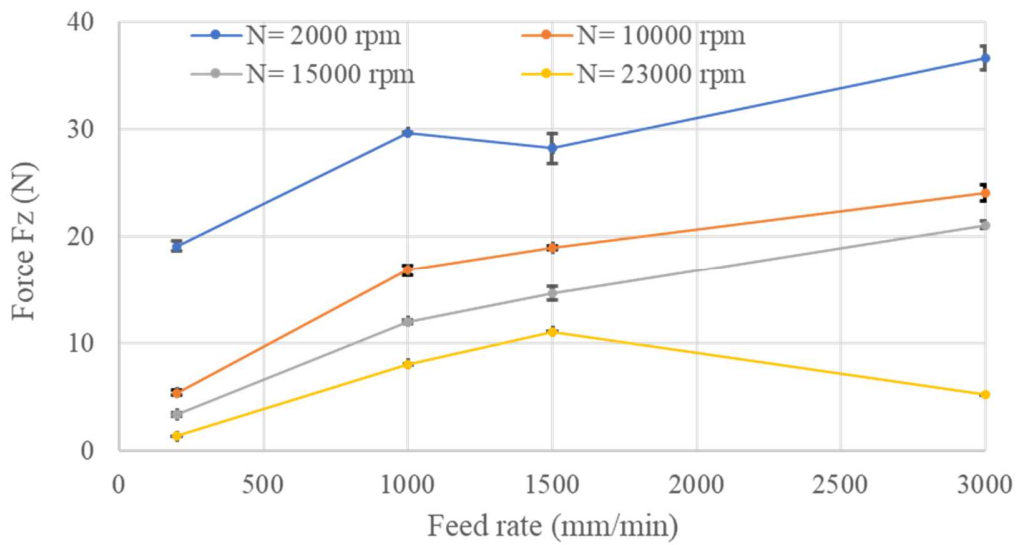
(a)



349

350

(b)



351

352

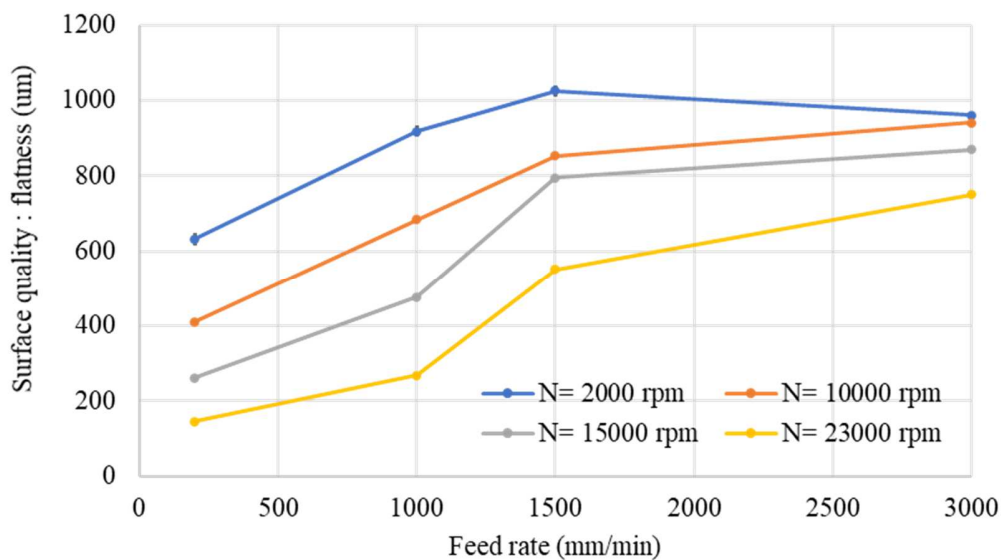
(c)

353 Figure 16. Evolution of milling forces for different cutting conditions for the combined tool
 354 CZ10: (a) F_x ; (b) F_y ; (c) F_z .

355 3.5. Analysis of the Nomex® honeycomb surface quality and induced damage

356 As said before, the degradations undergone exceed the limits of the roughness and reach the
357 criterion of shape defect. Thus, the correct machining of Nomex® will be justified by the small
358 size of flatness defect on the machined surface. This criterion is measured using the method
359 presented above.

360 Figure 17 illustrates the results of the effect of cutting conditions (feed rate and spindle speed) on
361 the quality of the machined surface. Generally, the size of defects increases with increasing the
362 feed rate and decreases with the cutting speed.

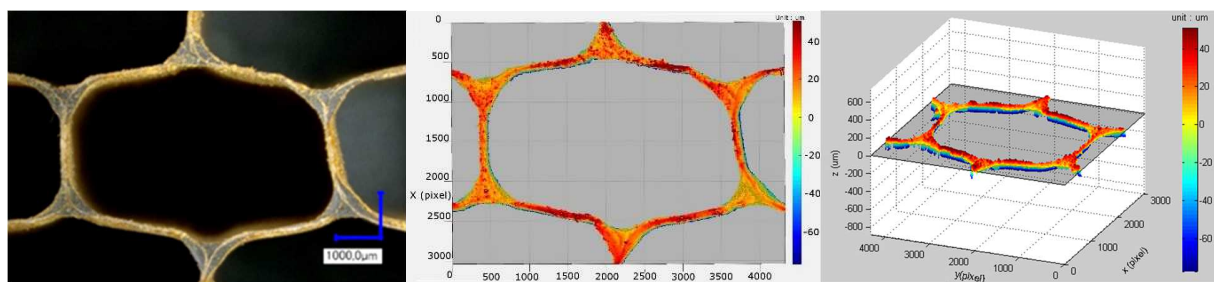


363
364 Figure 17. Evolution of surface defects with the feed rate and the spindle speed during the
365 machining of Nomex honeycomb with the combined CZ10 tool.

366 It should also be noted that the defects measured on the machined cells vary between 145 µm
367 and 1 mm. The damage generated during the machining of Nomex® exceeds the roughness
368 defect. The smallest defect size (about 145 µm) was observed for a spindle speed of 23000 rpm
369 and a feed rate of 200 mm/min. A saturation of surface defects was observed for all conditions

370 beyond 1500mm/min of the feed rate. This can be explained by a saturation of the tool wear
371 noticed for all cutting tools and under different cutting conditions.

372 Figure 18 presents an optical image of a machined cell under these conditions and the digital
373 processing performed on Matlab to calculate the size of the shape defect. There are no uncut
374 fibers nor tearing of the cell walls. A flat surface is observed with small differences between the
375 digitized points and the plane of least squares reference of the calculation. For the same spindle
376 speed (23000 rpm), the size of the defects increases with the feed rate to reach 751 μm with 3000
377 mm/min (a defect five times greater).



378

379

(a)

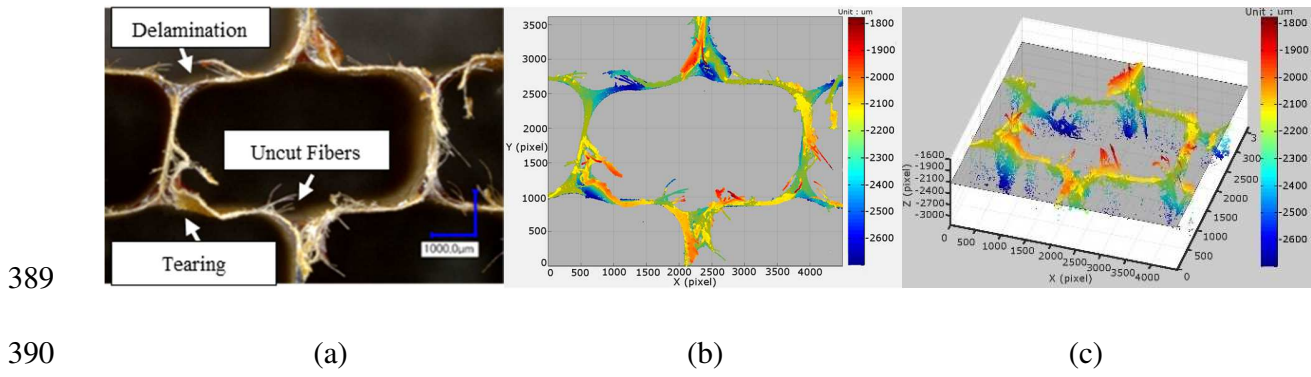
(b)

(c)

380 Figure 18. Machined surface for $N = 23000$ rpm and $f = 200$ mm/min: (a) optical image of a cell;
381 (b) 3D digital image; (c) Digital processing of the 3D image.

382 A defect size greater than 800 μm is synonymous with pronounced tearing of the honeycomb
383 walls as in the case of machining at low spindle speed (2000 rpm) and at high feed rate (3000
384 mm/min), Figure 19. There is an intense presence of uncut fibers, tearing of the simple walls and
385 delamination of junctions. The uncut fibers are located above the least squares plane (reference
386 plane for the calculation). The valleys caused by the tearing of the walls are below the reference

387 plane. This reflects the significant difference between the digitized points of the measured
388 surface and the least squares plane.



391 Figure 19. Machined surface for $N = 2000$ rpm and $f = 3000$ mm / min: (a) optical image of a
392 cell; (b) 3D digital image; (c) Digital processing of the 3D image.

393 Aramid fibers are difficult to cut because they are less fragile unlike other types of fibers used in
394 composite materials (as carbon or glass fibers). This gives a fluffy appearance to the honeycomb
395 cut walls. The length of uncut aramid fibers can be significant and, in some cases, can be seen
396 with naked eyes. For more details, see Table A11 in Appendix A in which all images related to
397 different cases of machining honeycomb are presented.

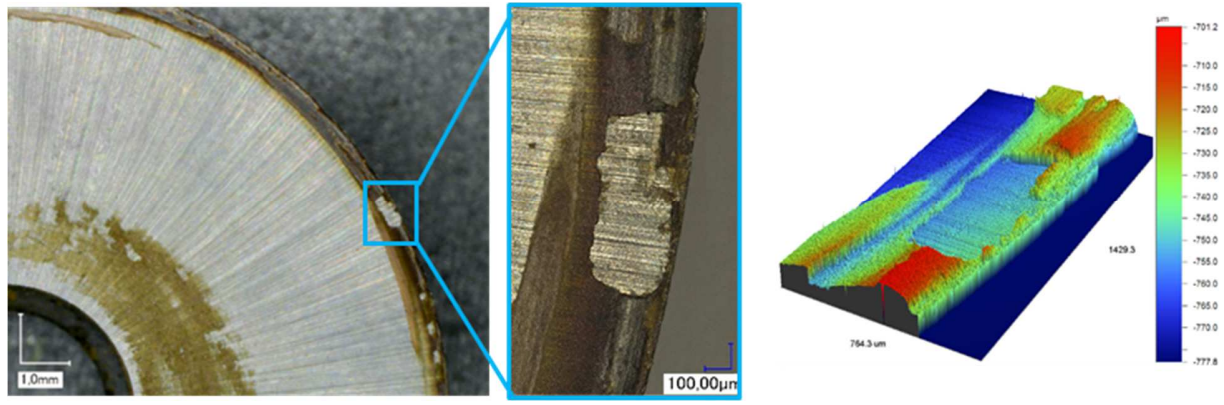
398 During the manufacture of sandwich materials, the meniscus created to maintain the structure
399 between the skin and the honeycomb can cover up to $300 \mu\text{m}$ of the walls [27,36]. This meniscus
400 height ensures optimal mechanical behavior of the sandwich structure. Thus, if the machining
401 defect exceeds $300 \mu\text{m}$, there is a great risk that the assembly of sandwich material will lead to
402 failure. The quality of accepted finish surface is that with a defect of less than $300 \mu\text{m}$. For this,
403 machining is recommended with a spindle speed greater than 15000 rpm and a feed rate less than

404 1000 mm/min. The higher the spindle speed and the lowest the feed rate, the better the quality is
405 for use in sandwich structures.

406 *3.6. Analysis of the tool wear and its effect on the surface quality*

407 Several tests have been set up to highlight the tool wear modes and their evolution according to
408 the cutting conditions. Nomex® honeycomb machining causes a yellowish powder to
409 accumulate on the combination tool. The color of this dust indicates that it comes from the
410 phenolic resin that coats the aramid paper. The accumulation of powder is more pronounced for
411 high spindle speed and low feed rate. This dust consists not only of phenolic resin but also of
412 aramid fibers cut into small fragments. A wear behavior similar to that observed during the
413 machining of conventional composite materials was found in our study. The observed wear
414 modes can be summarized as follow : (i)- bonding the resin to the tool, (ii)- flank wear and (iii)
415 loss of edge sharpness [37–39].

416 The saw blade is the most loaded tool element during the milling operation. It has a direct effect
417 on the machined surface and plays the role of cutting and separating the walls of Nomex® to
418 generate chips. To check its resistance to the stresses of milling, in-depth observations of the
419 state of the lower surface of the saw blade (flank surface) are made. This analysis showed a
420 deposit of material on the flank surface of the saw blade, which is in permanent contact with the
421 machined surface, Figure 20. The thickness of the strip can exceed 50 µm. The topographic
422 analysis also shows the detachment on certain areas of the strip resin. The surface of the flank
423 surface in these areas is intact and does not show any removal of material, which favors the
424 hypothesis of sticking of the material on the saw blade edge.



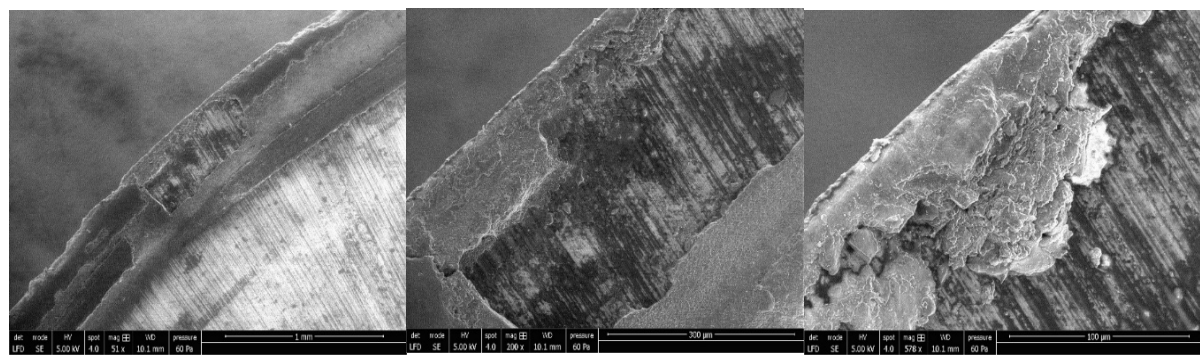
425

426

(a) (b) (c)

427 Figure 20. Topographic analysis of the bonding strip on the flank surface of the saw blade: (a)
 428 Optical image; (b) Zoom on the gluing strip; (c) 3D topography.

429 Additional analyzes were performed using a scanning electron microscope (SEM) under
 430 pressure. In Figure 21, it can be seen an accumulation of the material near to the cutting tool
 431 edge. The stacking of the layers of resin on top of each other contributes to an increase in the
 432 bonding deposit. This proves an increase in temperature at the honeycomb walls and the tool
 433 which reaches a transition temperature to the viscous state of the phenolic resin.



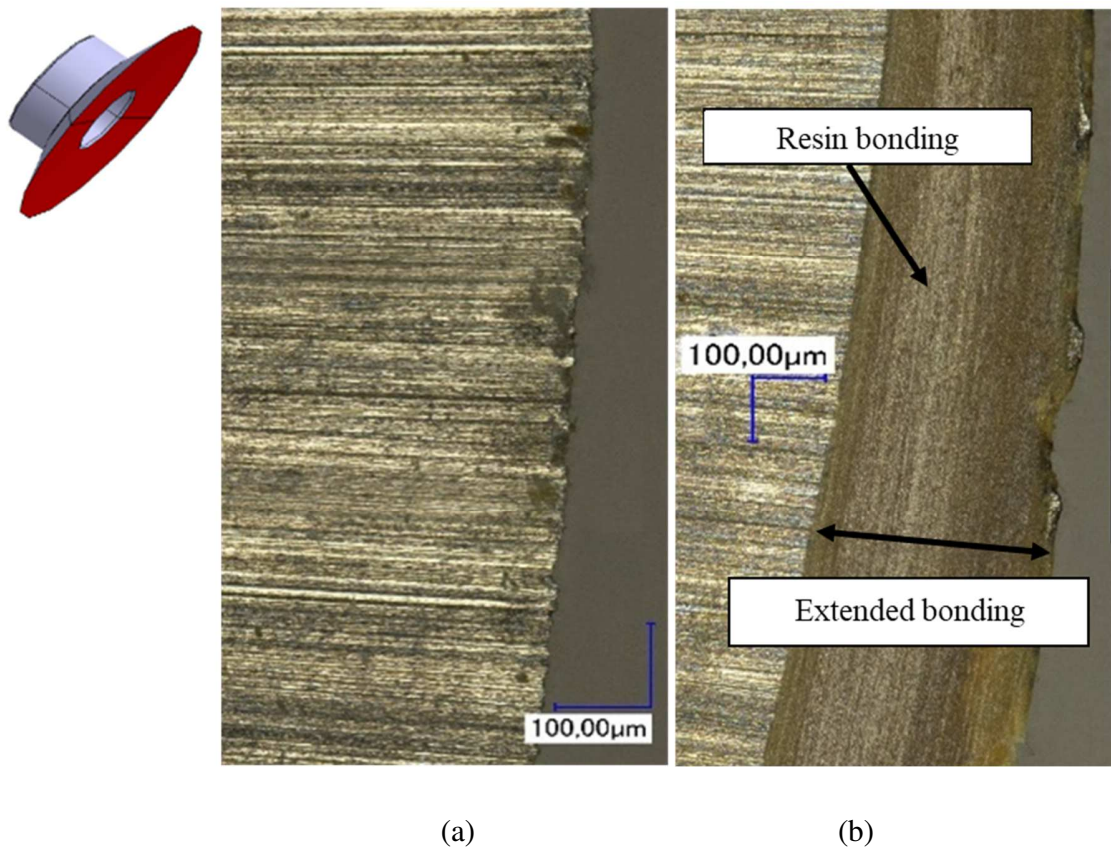
434

435

(a) (b) (c)

436 Figure 21. SEM observations of the adhesive strip on the flank surface of the saw blade: (a)
 437 zoom x51; (b) x200 zoom; (c) x578.

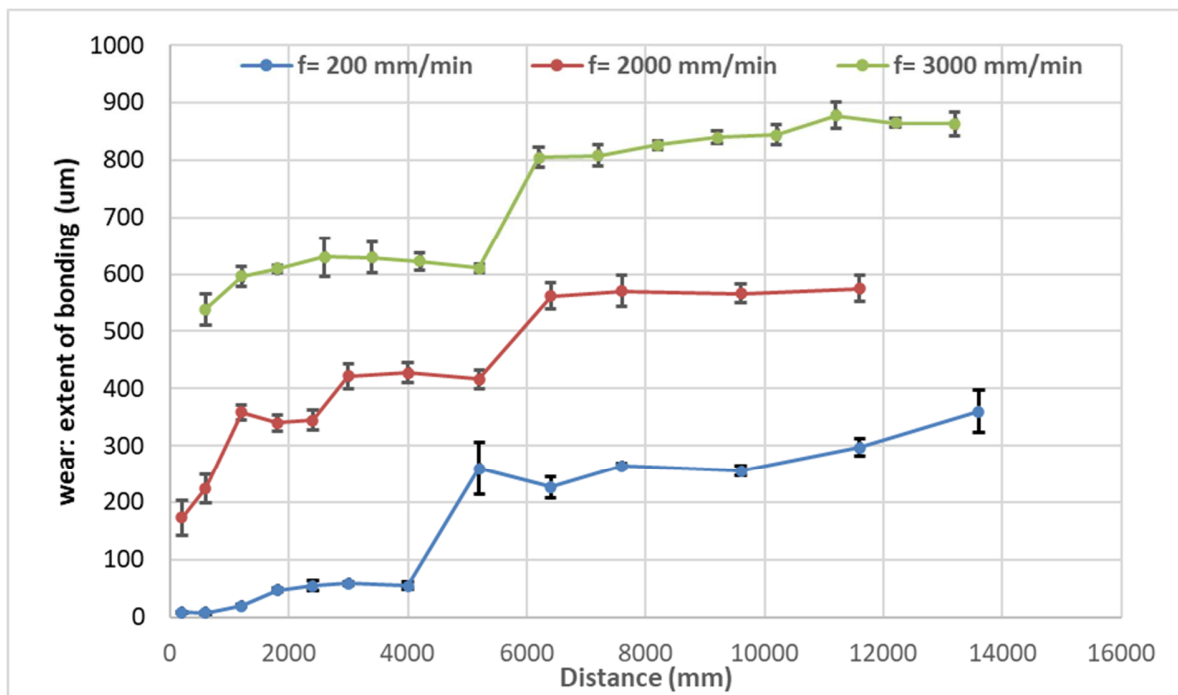
438 Nomex® honeycomb milling tests were performed to study the influence of milling conditions
439 on tool wear. We have considered the machining length for each tool as the pertinent parameter
440 to analyze the wear process. Thus, the extent of bonding was measured as a function of the
441 distance traveled by the tool during machining, Figure 22.



444 Figure 22. Identification of the extent of resin bonding (a) new tool; (b) worn tool.

445 Figure 23 shows the evolution of the extended bonding as a function of the machining length for
446 three cutting conditions. The wear is more pronounced for a feed rate of 3000 mm/min, the
447 extent of the bonding area is 538 µm from the start of machining. The shape of the wear curve
448 changes slowly at the beginning of machining and forms a first plateau until it reaches a critical

449 length of 5.2 m. A severe increase in the bonding area is recorded, reaching a value of 800 μm .
 450 Subsequently, a second plateau is observed, it is linked to the moderate increase in the extent of
 451 the bonding area. The same trend is noted for the other two conditions of the curve. The wear
 452 level is lower for low feed rates (200 mm/min). It begins at a few micrometers until it reaches a
 453 value of 360 μm for a machining length of 13.6 m with an abrupt increase in wear observed at a
 454 length of 4 m. This sudden increase is noted for the case of a feed rate 2000 mm/min at a length
 455 of 5.2 m. Wear by bonding on the flank surface goes through three stages: weak evolution of
 456 bonding, aggressive increase in the width of the adhesive strip and finally return to stabilization
 457 with a plateau.



458

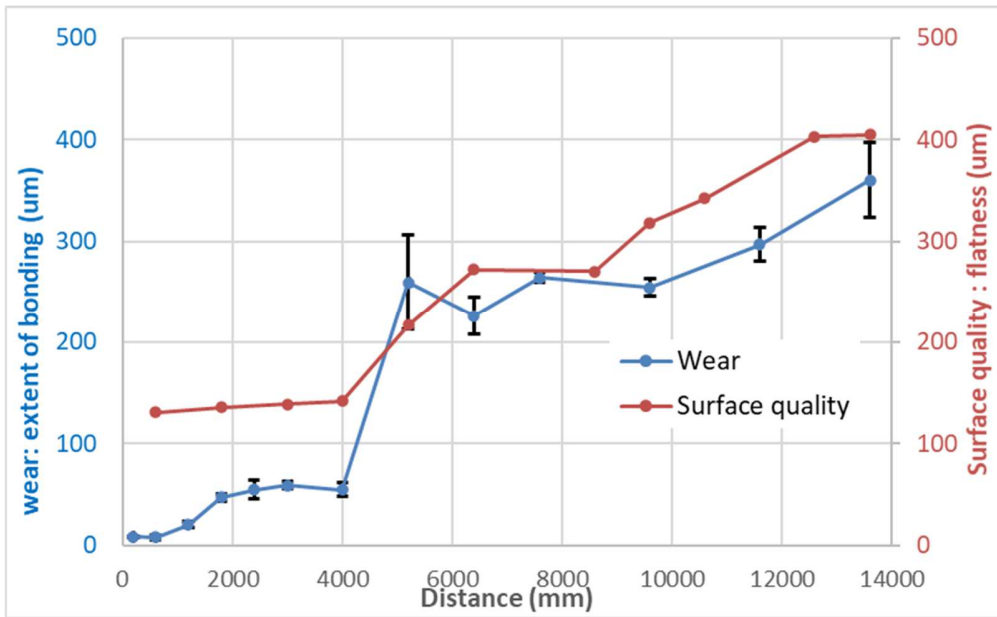
459

Figure 23. Evolution of wear as a function of the machined length, $N= 23000$ rpm.

460 Generally, tool wear leads to an increase in cutting forces and cutting temperatures and a
461 deterioration of the surface quality. These cause a decrease in the precision of the finished piece,
462 modification of the tool geometry and a tool break. Figure 24 shows a comparison between wear
463 and the surface quality. It can be noticed that the evolution of the surface quality is proportional
464 to that of the tool wear. When wear stagnates, the surface defect remains almost constant, thus, a
465 plateau at the curve is observed, Figure 24.a. For $f = 200$ mm/min, surface quality starts at 130
466 μm and the stagnation plateau ends with a value of 141 μm after 4 m of cutting length, Figure
467 24.a, at this distance the wear is suffered a severe increase in the bonding range from 55 μm to
468 260 μm , this increase causes an increase in the flatness defect on the machined surface where it
469 doubles to reach a value of 272 μm after 6.4 m traversed by the tool. A second short plateau of
470 stagnation can be also observed at 6.4 m and then the surface quality deteriorates to reach the
471 value of 405 μm at a distance of 13.6 m. This increase is caused by the increase in the bonding
472 area on the flank surface which goes from 254 μm for 9.6 m distance to 360 μm at the end of the
473 measurement. The same behavior of wear and surface quality can be observed for the two other
474 feed rates. For $f = 2000$ mm/min, the surface defect begins at 768 μm for a bonding range of 358
475 μm , a severe increase in wear and surface defect is observed at a distance of 5.2 m to reach a
476 surface defect of 972 μm and wear of 561 μm , Figure 24.b. For $f = 3000$ mm/min, the first
477 plateau is observed up to a distance traversed by the tool of 5.2 m with a wear of 622 μm and a
478 flatness defect of 870 μm , the second stagnation plateau is characterized by a surface defect of
479 1.1 mm and a bonding area of 1.09 mm, Figure 24.c.

480

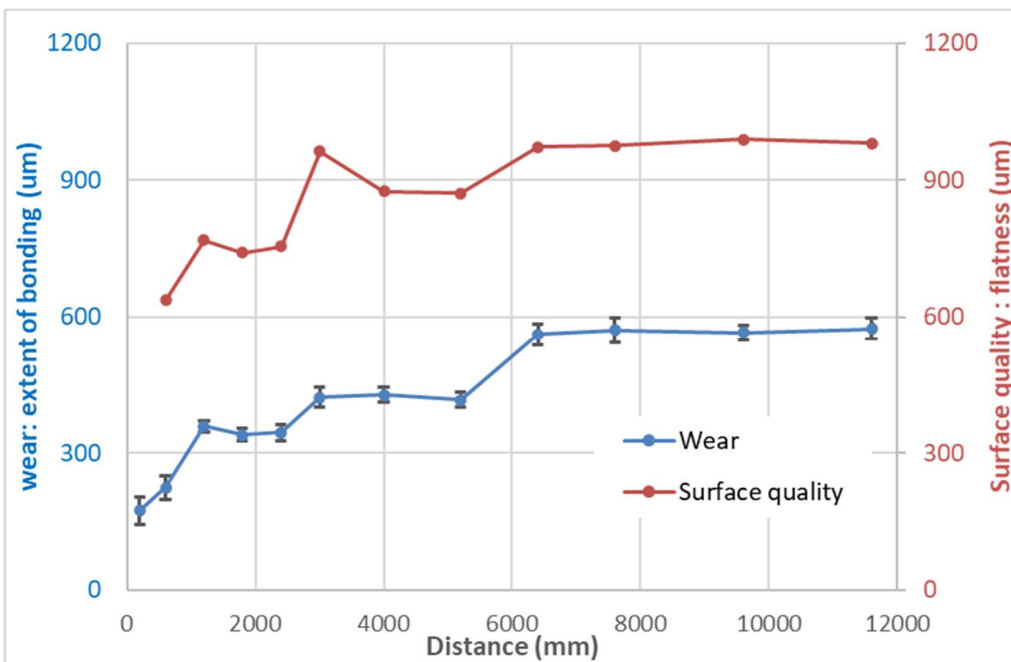
481



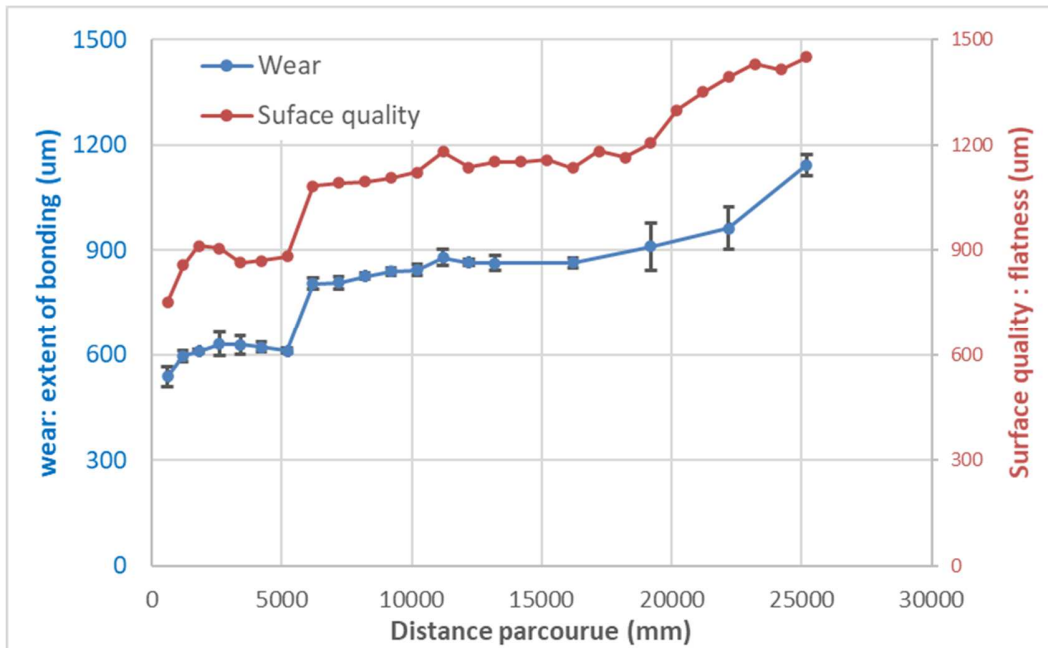
(a)

482

483



(b)



484

485

(c)

486

Figure 24. Evolution of the tool wear and surface quality versus machining length, $N= 23000$

487

rpm: (a) $f= 200$ mm/min; (b) $f=2000$ mm/min; (c) $f= 3000$ mm/min.

488

Knowing that the limit of the authorized flatness defect to have a good assembly of the sandwich

489

structure with a honeycomb core is about $300 \mu\text{m}$, it is not advised to machine more than 9 m

490

with the combined tool with a spindle speed of 23000 mm/min and a feed rate of 200 mm/min.

491

Above this distance the flatness defect becomes greater than $300 \mu\text{m}$.

492

The evolution of the bonding extent is done by the accumulation of phenolic resin layers on the

493

top of each other. The accumulation of resin on the flank surface of the saw blade causes a

494

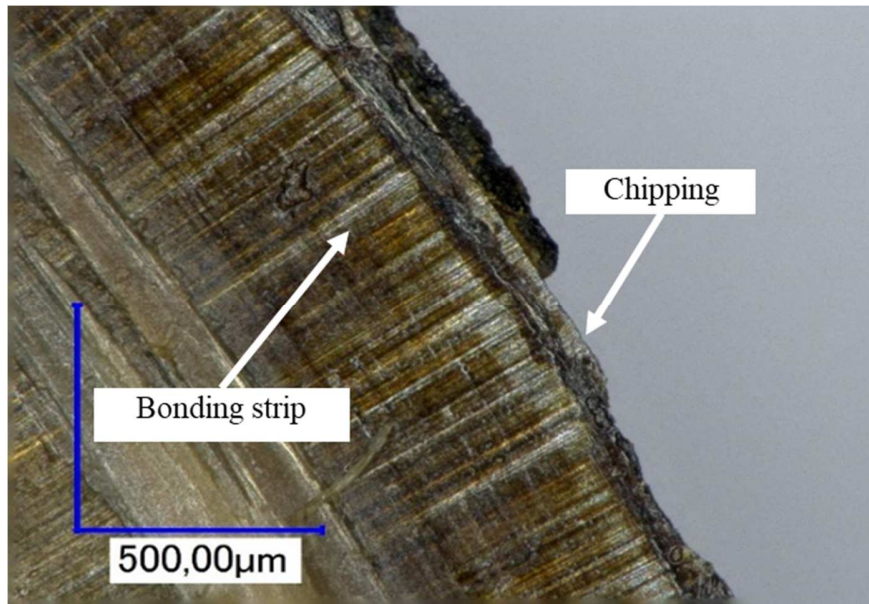
change in the tool geometry and concentrates stresses on the tool. This weakens the cutting edge

495

as for the built-up edge effect in the case of machining usual materials (as aluminums, CFRP

496

composites,...). This process ends with breakage and flaking of the cutting edge, Figure 25.



497

498 Figure 25. Occurrence of chipping due to the sticking of the resin on the saw blade edge. The
499 considered cutting conditions are : $N = 23,000$ rpm; $f = 200$ mm/min; machining length 13.6 m.

500

501 4. Conclusion

502 When machining the NOMEX® honeycomb structures, the poor surface quality is characterized
503 by the tearing of the cell walls and uncut or fully torn fibers. Geometrical and surface roughness
504 analyses are limited to classical materials and then they are not valid for the honeycomb
505 structures due to their alveolar shape. To overcome this limitation, a new and innovative protocol
506 was developed to analyze measurements of the surface parameters and to precisely evaluate the
507 machined surface quality. This protocol allows to measure the size of defects generated by the
508 geometric constraints of the surface. Thus, it is possible to carry out an in-depth analysis of the
509 cutting conditions influence as the feed rate and spindle speed on the quality of obtained surfaces
510 by machining process. It has been found that low feed rate and high spindle speed make it
511 possible to reduce the cutting induced damage or even eliminate the surface defects of

512 honeycombs. The quality of the surface degrades by increasing the feed rate and/or by
513 decreasing the spindle speed. Under these conditions, there is a tearing of the walls with uncut
514 fibers of very large size. For the tested Nomex® samples, the optimal condition is found with
515 high spindle speed (23,000 rpm) and low feed rate (200 mm/min).

516 The wear is exhibited by a bonding of the phenolic resin constituting the cell walls on the flank
517 surface of the saw blade. It was observed for high spindle speeds an increase in the local
518 temperature which favor the bonding of the resin on the flank face of the saw blade. Adhesive
519 layers of the phenolic resin form on the surface of the tool and contribute to its damage. This
520 phenomenon is favored by the low thermal conductivity of the composites and therefore by the
521 heat generated by the friction process of the tool on the cell walls. The evolution of tool wear
522 leads to the degradation of the surface quality during machining. Thus, less frank cuts of the
523 walls and the tearing of the fibers can be observed.

524 **Acknowledgments**

525 The authors wish to express their thanks and appreciation to members of the following
526 organizations for their financial support: Evatec-tools group and National French Research
527 Agency (ANR). LARIOPAC LabCom project under Grant No. ANR-13-LAB2-0002.

528

529 **References**

- 530 [1] Cognard P. Collage des composites - Secteur aéronautique. Tech l'ingénieur
531 2012;BM7626 V1.
- 532 [2] Bitzer T. Honeycomb Technology. Dordrecht: Springer Netherlands; 1997.
533 <https://doi.org/10.1007/978-94-011-5856-5>.

- 534 [3] Fischer S, Drechsler K, Kilchert S, Johnson A. Mechanical tests for foldcore base material
535 properties. *Compos Part A* 2009;40:1941–52.
536 <https://doi.org/10.1016/j.compositesa.2009.03.005>.
- 537 [4] Foo CC, Chai GB, Seah LK. Mechanical properties of Nomex material and Nomex
538 honeycomb structure. *Compos Struct* 2007;80:588–94.
539 <https://doi.org/10.1016/j.compstruct.2006.07.010>.
- 540 [5] Kim DS, Lee JR. Compressive mechanical properties of the nomex/thermoset honeycomb
541 cores. *Polym Adv Technol* 1997;8:1–7. [https://doi.org/10.1002/\(SICI\)1099-1581\(199701\)8:1<1::AID-PAT601>3.0.CO;2-G](https://doi.org/10.1002/(SICI)1099-1581(199701)8:1<1::AID-PAT601>3.0.CO;2-G).
- 543 [6] Zinno A, Prota A, Di Maio E, Bakis CE. Experimental characterization of phenolic-
544 impregnated honeycomb sandwich structures for transportation vehicles. *Compos Struct*
545 2011;93:2910–24. <https://doi.org/10.1016/j.compstruct.2011.05.012>.
- 546 [7] Aminanda Y, Castanie B, Barrau JJ, Thevenet P. Experimental and numerical study of
547 compression after impact of sandwich structures with metallic skins. *Compos Sci Technol*
548 2009;69:50–9. <https://doi.org/10.1016/j.compscitech.2007.10.045>.
- 549 [8] Hu LL, Yu TX. Dynamic crushing strength of hexagonal honeycombs. *Int J Impact Eng*
550 2010;37:467–74. <https://doi.org/10.1016/j.ijimpeng.2009.12.001>.
- 551 [9] Wang ZW, E YP. Mathematical modelling of energy absorption property for paper
552 honeycomb in various ambient humidities. *Mater Des* 2010;31:4321–8.
553 <https://doi.org/10.1016/j.matdes.2010.03.053>.
- 554 [10] Papka SD, Kyriakides S. Biaxial crushing of honeycombs Part I: Experiments. *Int J*
555 *Solids Struct* 1999;36:4367–96.
- 556 [11] Suwannarungsri L, Tanthapanichakoon W. Test production of honeycomb structure using
557 simple practical equipment. *Proc MS* 2006:D08.
- 558 [12] Hexcel Composites. Honeycomb Attributes and Properties, A comprehensive guide to
559 standard Hexcel honeycomb materials, configurations, and mechanical properties.
560 *Honeycomb Data Sheets* 1999:1–40.
- 561 [13] DESSARTHE A. Usinage des composites. *Tech l'ingénieur* 1997;33:215.
- 562 [14] Nasedkin Y V., Tsarev VF, Zelenina I V. Cutting of aramide fiber-reinforced plastics by
563 Co2 laser. *Mech Compos Mater* 1999;35:259–264.
564 <https://doi.org/10.1117/1.JMM.13.2.023012>.
- 565 [15] Norvilie HS, Madera C, Tibor E. Process for machining expanded honeycomb. U.S.
566 Patent No 3,413,708, 1968.
- 567 [16] S.Nilsen J, Wadsworth O. Method and apparatus for machining and for holding during

- 568 machining honeycomb material. Patent Number : 2905064, 1959.
- 569 [17] Griffith CG, Herbert JTA. Method of machining honeycomb core. U.S. Patent No
570 2,855,664, 1958.
- 571 [18] Carl R, Vista C. Three-dimensional honeycomb core machining apparatus and method.
572 US 2014/0161553 A1, 2014.
- 573 [19] Hirayama A. Method for cutting honeycomb core. U.S. Patent No 6,740,268, 2004.
- 574 [20] Thiagaraj R, Chris RM, McCullough JR, Mishra S. Method of repairing, splicing, joining,
575 machining, and stabilizing honeycomb core using pourable structural foam and a structure
576 incorporating the same. US 20140120305 A1, 2014.
- 577 [21] Jaafar M, Atlati S, Makich H, Nouari M, Moufki A, Julliere B. A 3D FE Modeling of
578 Machining Process of Nomex® Honeycomb Core: Influence of the Cell Structure
579 Behaviour and Specific Tool Geometry. *Procedia CIRP* 2017;58:505–10.
580 <https://doi.org/10.1016/j.procir.2017.03.255>.
- 581 [22] Qin Y, Kang R, Dong Z, Wang Y, Yang J, Zhu X. Burr removal from measurement data
582 of honeycomb core surface based on dimensionality reduction and regression analysis.
583 *Meas Sci Technol* 2018;29. <https://doi.org/10.1088/1361-6501/aae1c4>.
- 584 [23] Grove SM, Popham E, Miles ME. An investigation of the skin/core bond in honeycomb
585 sandwich structures using statistical experimentation techniques. *Compos Part A Appl Sci*
586 *Manuf* 2006;37:804–12. <https://doi.org/10.1016/j.compositesa.2005.07.005>.
- 587 [24] Heimbs S. Sandwichstrukturen mit Wabenkern: Experimentelle und numerische Analyse
588 des Schädigungsverhaltens unter statischer und kurzzeitdynamischer Belastung. Institut
589 für Verbundwerkstoffe GmbH, 2008.
- 590 [25] Tchoutouo H, Gandy N. Adhesiveless honeycomb sandwich structure with carbon
591 graphite prepreg for primary structural application: a comparative study to the use of
592 adhesive film. Thesis, Department of Mechanical Engineering and the faculty of the
593 Graduate School of Wichita State University, 2012.
- 594 [26] Davis MJ, McGregor A. The importance of failure mode identification in adhesive bonded
595 aircraft structures and repairs. *Int Conf Compos Mater* 1999:5–9.
- 596 [27] Rion J, Leterrier Y, Manson JE. Prediction of the adhesive fillet size for skin to
597 honeycomb core bonding in ultra-light sandwich structures. *Compos Part A*
598 2008;39:1547–55. <https://doi.org/10.1016/j.compositesa.2008.05.022>.
- 599 [28] Mendoza MM, Eman KF, Wu SM. Development of a new milling cutter for aluminium
600 honeycomb. *Int J Mach Tool Des Res* 1983;23:81–91. [https://doi.org/10.1016/0020-7357\(83\)90009-4](https://doi.org/10.1016/0020-7357(83)90009-4).
601

- 602 [29] Geng D, Zhang D, Xu Y, He F, Liu D, Duan Z. Rotary ultrasonic elliptical machining for
603 side milling of CFRP: Tool performance and surface integrity. *Ultrasonics* 2015;59:128–
604 37. <https://doi.org/10.1016/j.ultras.2015.02.006>.
- 605 [30] Nor Khairusshima MK, Che Hassan CH, Jaharah a. G, Amin a. KM, Md Idriss a. N.
606 Effect of chilled air on tool wear and workpiece quality during milling of carbon fibre-
607 reinforced plastic. *Wear* 2013;302:1113–23. <https://doi.org/10.1016/j.wear.2013.01.043>.
- 608 [31] Zitoune R, El Mansori M, Krishnaraj V. Tribo-functional design of double cone drill
609 implications in tool wear during drilling of copper mesh/CFRP/woven ply. *Wear*
610 2013;302:1560–7. <https://doi.org/10.1016/j.wear.2013.01.046>.
- 611 [32] Haddad M, Zitoune R, Bougherara H, Eyma F, Castanié B. Study of trimming damages of
612 CFRP structures in function of the machining processes and their impact on the
613 mechanical behavior. *Compos Part B Eng* 2014;57:136–43.
614 <https://doi.org/10.1016/j.compositesb.2013.09.051>.
- 615 [33] Saleem M, Toubal L, Zitoune R, Bougherara H. Investigating the effect of machining
616 processes on the mechanical behavior of composite plates with circular holes. *Compos*
617 *Part A Appl Sci Manuf* 2013;55:169–77.
618 <https://doi.org/10.1016/j.compositesa.2013.09.002>.
- 619 [34] Teti R. Machining of Composite Materials. *CIRP Ann - Manuf Technol* 2002;51:611–34.
620 [https://doi.org/10.1016/S0007-8506\(07\)61703-X](https://doi.org/10.1016/S0007-8506(07)61703-X).
- 621 [35] Wang H, Sun J, Li J, Lu L, Li N. Evaluation of cutting force and cutting temperature in
622 milling carbon fiber-reinforced polymer composites. *Int J Adv Manuf Technol*
623 2016;82:1517–25. <https://doi.org/10.1007/s00170-015-7479-2>.
- 624 [36] Rion J, Leterrier Y, Demarco F, Manson JAE. Damage analysis of ultralight composite
625 sandwich structures. *ICCM Int Conf Compos Mater* 2007;1:1–6.
- 626 [37] Rawat S, Attia H. Wear mechanisms and tool life management of WC–Co drills during
627 dry high speed drilling of woven carbon fibre composites. *Wear* 2009;267:1022–30.
628 <https://doi.org/10.1016/j.wear.2009.01.031>.
- 629 [38] Faraz A, Biermann D, Weinert K. Cutting edge rounding: An innovative tool wear
630 criterion in drilling CFRP composite laminates. *Int J Mach Tools Manuf* 2009;49:1185–
631 96. <https://doi.org/10.1016/j.ijmactools.2009.08.002>.
- 632 [39] Park KH, Beal A, Kim DDW, Kwon P, Lantrip J. Tool wear in drilling of
633 composite/titanium stacks using carbide and polycrystalline diamond tools. *Wear*
634 2011;271:2826–35. <https://doi.org/10.1016/j.wear.2011.05.038>.

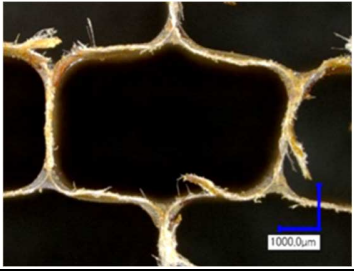
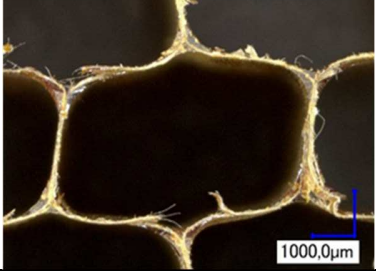
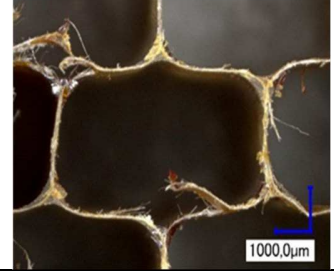
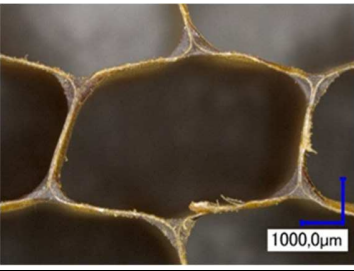
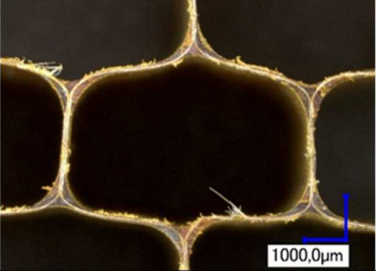
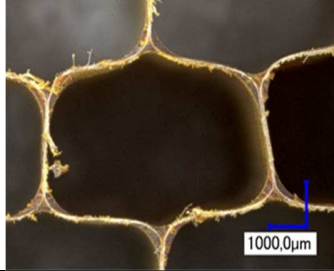
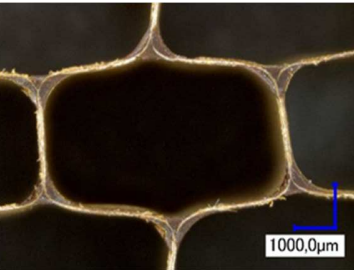
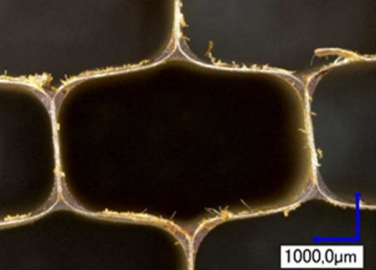
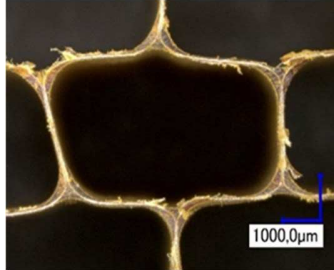
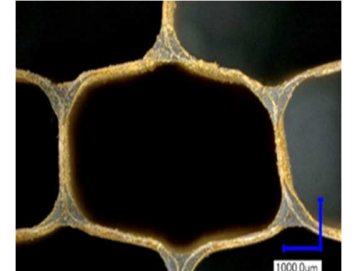
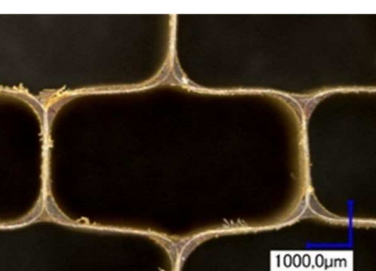
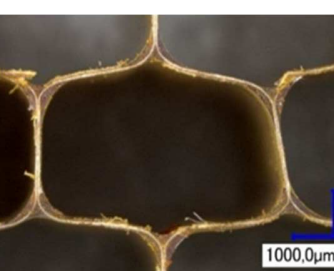
635

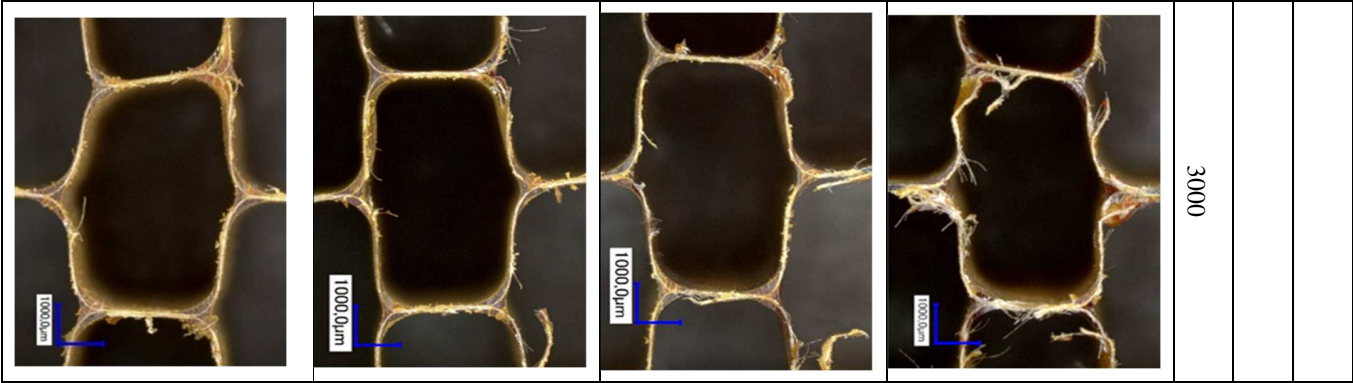
636

637
638
639

APPENDIX A

Tableau A1. Optical microscope images of honeycomb cells machined under various cutting conditions.

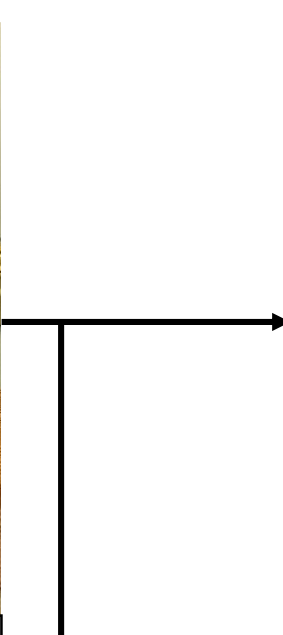
		Feed rate f (mm/min)		
		200	1000	1500
Spindle speed (cutting speed), N (tr/min)	2000			
	10000			
	15000			
	23000			



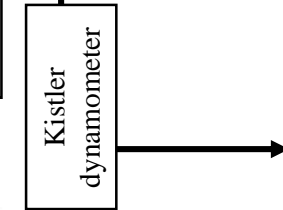
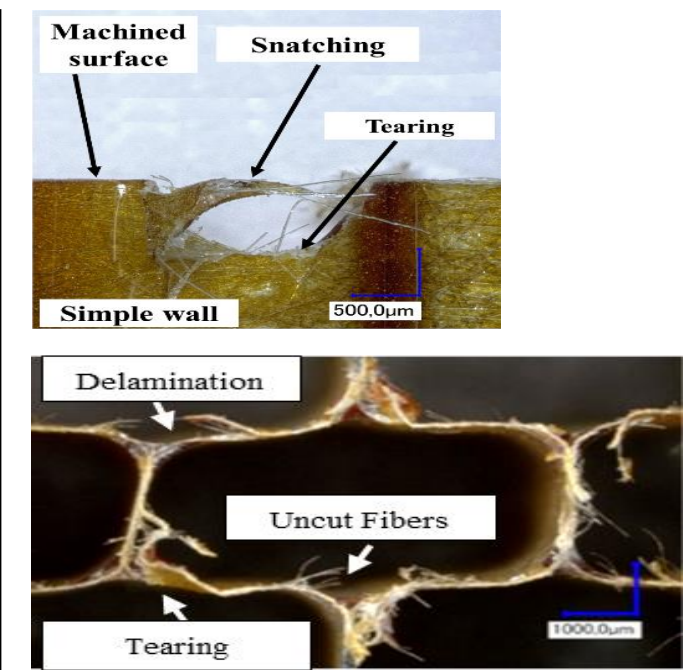
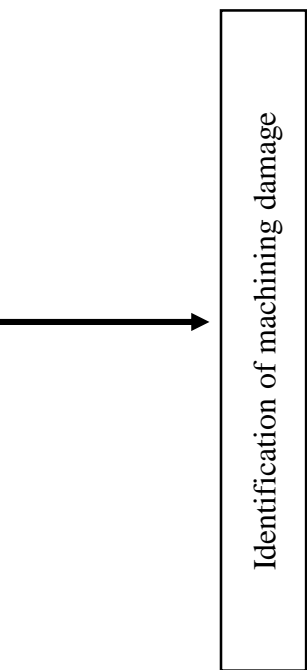
640



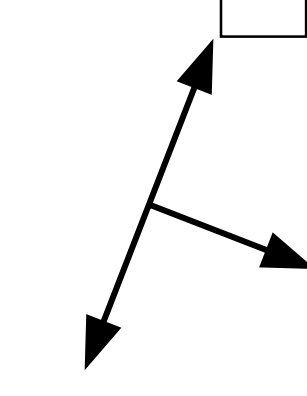
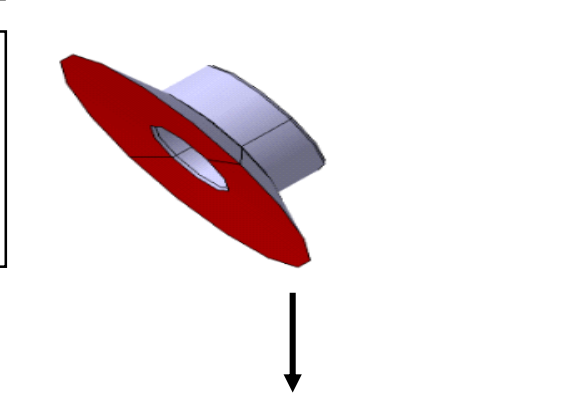
Machining Nomex Honeycomb



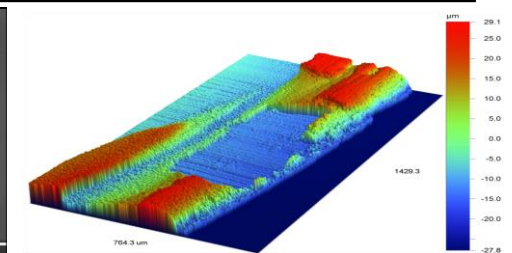
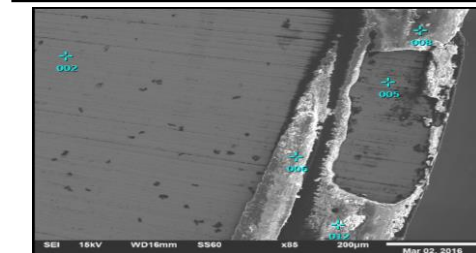
Observation of surface quality



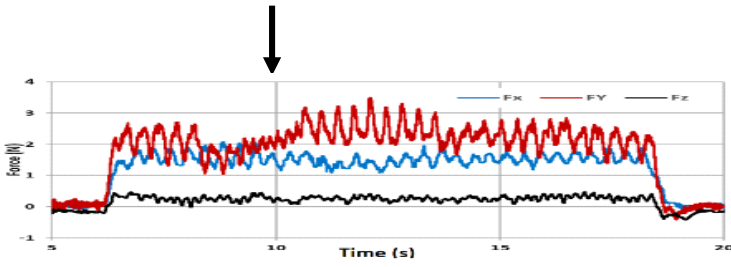
Tool wear



Type and evolution of wear



Kistler dynamometer



Monitoring of cutting forces

- Understanding of honeycomb cutting
- Determination of optimal cutting conditions
- Establishment of a method for measuring surface quality
- Correlation between wear and surface quality